Highly oxidized intraplate basalts and deep carbon storage

Xu-Han Dong[1], Shui-Jiong Wang[1*, 2], Wenzhong Wang[3*, 4, 5], Shichun Huang[6], Qiu-Li Li[7], Chengshuai Liu[8], Ting Gao[8], Shuguang Li[1], Shitou Wu[7]

Affiliations:

[1] *State Key Laboratory of Geological Processes and Mineral Resources, China University of Geosciences (Beijing), Beijing 100083, China*

[2] *Frontiers Science Center for Deep-time Digital Earth, China University of Geosciences (Beijing), Beijing, 100083, China*

[3] *Deep Space Exploration Laboratory / School of Earth and Space Sciences, University of Science and Technology of China, Hefei 230026, China*

[4] *CAS Center for Excellence in Comparative Planetology, USTC, China*

[5] *National Geophysical Observatory at Mengcheng, USTC, China*

[6] *Department of Earth, Environmental, & Planetary Sciences, University of Tennessee, Knoxville, TN 37996-1410, USA*

[7] *State Key Laboratory of Lithospheric Evolution, Institute of Geology and Geophysics, Chinese Academy of Sciences, Beijing 100029, China*

[8] *State Key Laboratory of Environmental Geochemistry, Institute of Geochemistry, Chinese Academy of Sciences, Guiyang 550081, China*

2nd revision submitted to Science Advances, May 7th, 2024

*Corresponding authors:

wsj@cugb.edu.cn (S.-J. Wang); wwz@ustc.edu.cn (W.-Z. Wang)

Abstract

The deep carbon cycle plays a critical role in mantle dynamic and maintaining Earth's habitability. Recycled carbonates are a strong oxidant in mantle carbon-iron redox reactions, leading to the formation of highly oxidized mantle domains and deep carbon storage. Here we report high $Fe^{3+}/\sum Fe$ values in Cenozoic intraplate basalts from eastern China, which are correlated with geochemical and isotopic compositions that point to a common role of carbonated melt with recycled carbonate signatures. We propose that the mantle source of these highly oxidized basalts has been oxidized by carbonated melts derived from the stagnant subducted slab in the mantle transition zone beneath eastern China. Diamonds formed during the carbon-iron redox reaction were separated from the melt due to density difference. This would leave a large amount of carbon (~four times of pre-industrial atmospheric carbon budget) stored in the deep mantle and isolated from global carbon cycle. As such, the amounts of subducted slabs stagnated at mantle transition zone can be an important factor regulating the climate.

Teaser

Intraplate basalts contain a highly oxidized mantle endmember rooted at the mantle transition zone.

INTRODUCTION

The mantle oxidation state plays a crucial role shaping our Earth, both its solid interior and atmosphere. In an isochemical mantle, the redox state decreases with increasing depth (*1*). However, this simple relationship can be disrupted by crustal recycling (*2*). For instance, deeply sourced, incompatible element enriched intraplate basalts, such as ocean island basalts (OIB), are more oxidized than mid-ocean ridge basalts (MORB) that sample the shallow depleted mantle (*2-4*). The presence of high-$Fe^{3+}/\sum Fe$ (up to 0.85) inclusions trapped within superdeep diamonds (*5, 6*) also hints for highly oxidized deep (>250 km) mantle domains formed by carbon-iron redox reaction (*7, 8*). However, the exact role of the proposed carbon-iron redox reaction in the petrogenesis of highly oxidized intraplate basalts remains to be explored.

The Pacific slab is subducting westwards along the Japan-Izu-Bonin-Mariana arc (Fig. 1B) (*9*). Seismic tomography reveals that the subducted Pacific slab is now stagnated horizontally at the mantle transition zone (MTZ) beneath eastern China (EC), extending up to 1600 km west of the subduction zone. The mantle region above the stagnated subducted Pacific slab is referred to as the Big Mantle Wedge (BMW) (*10*), which has been fully developed since early Cretaceous (*11, 12*). The widespread, voluminous Cenozoic intraplate volcanism (~79,000 km^2) in EC is thus not associated with mantle plumes or arcs (*13-15*) (Fig. 1A, B). Rather, they are related to partial melting of the BMW beneath EC triggered by fluids/melts released from the subducted Pacific slab stagnated at MTZ, during which subducted marine carbonates and carbonated oceanic crust may have played a key role (*13-16*).

The intraplate basalts from EC range from nephelinite to basaltic andesite in a total alkali vs silica (TAS) diagram (Supplementary Fig. 1 and Supplementary Section 1 for Materials). In a PM (primitive mantle)-normalized trace element diagram, the EC basalts have trace element patterns like OIB with HIMU (high μ, $\mu = {}^{238}U/{}^{204}Pb$) affinity (Fig. 1C) (*17*). Their $^{206}Pb/^{204}Pb$ ratios range from 16.6 to 19.0, lower than typical HIMU basalts, suggesting a young recycled oceanic component in the source (*13*).

Here, we measured the bulk rock $Fe^{3+}/\sum Fe$ and olivine $\delta^{18}O$ values in 42 well-studied Cenozoic intraplate basalts from eastern China. The studied Cenozoic EC basalts have $Fe^{3+}/\sum Fe$ values up to 0.6, much higher than those observed in MORB (0.14 ± 0.01; 1σ) (*18*) and OIB (from 0.16 to 0.4) (*19, 20*). The high $Fe^{3+}/\sum Fe$ values are well correlated with olivine $\delta^{18}O$ and V/Sc values, as well as bulk rock elemental and stable isotopic characteristics that are best explained as a result of carbon-iron redox reaction involving carbonated melts from subducted slab at the MTZ. We also employed first-principles molecular dynamics calculations to constrain the melt-diamond density crossover in the mantle. We found that during carbon-iron redox reaction, diamonds are denser than melts, and, consequently, can be efficiently separated from the melts due to density difference. This reaction has facilitated deep carbon storage at the MTZ and formed a highly oxidized mantle endmember (HOME) which contributes significantly to intraplate basalts.

RESULTS

The $Fe^{3+}/\sum Fe$ ratios of EC basalts are unusually high, ranging from 0.11 to 0.6. Duplicate wet-chemistry $Fe^{3+}/\sum Fe$ measurements of individual samples agree with each other within ± 3% (RSD) (Supplementary Table 1). Geological rock references of BCR-2, BHVO-2, GSR-1, GSR-2 and GSR-3 measured as unknowns yield $Fe^{3+}/\sum Fe$ values of 0.21, 0.25, 0.48, 0.47 and 0.38, respectively, consistent with their certified values within ± 10% (Supplementary Table 2). A subset of samples covering the entire range of $Fe^{3+}/\sum Fe$ were analyzed using Mössbauer

spectroscopy (Supplementary Fig. 2 for Mössbauer spectra), and the Mössbauer results agree well with the wet-chemical $Fe^{3+}/\sum Fe$ within ±10% (Fig. 2A).

Measured $\delta^{18}O$ values of phenocrystic olivines in EC basalts (from +5.2‰ to +4.2‰) are slightly lower than or comparable to the upper mantle estimate (+5.5 ± 0.2‰) (*21*). The vanadium-to-scandium (V/Sc) ratios of olivines vary from 0.88 to 2.27 (Supplementary Table 4), systematically lower than the average of primitive mantle (V/Sc = 4.9) (*22*). No intra-grain variations in $\delta^{18}O$, V or Sc were observed (Supplementary Fig. 3). The olivine-$\delta^{18}O$ and V/Sc are well correlated with the bulk-rock $Fe^{3+}/\sum Fe$ values, with high-$Fe^{3+}/\sum Fe$ samples having higher $\delta^{18}O$ and lower V/Sc ratios (Fig. 2B, C).

DISCUSSION

High $Fe^{3+}/\sum Fe$ of EC basalt

There are several shallow processes that could potentially affect the bulk rock $Fe^{3+}/\sum Fe$. We assess the effect of these processes below and provide compelling evidence that the high $Fe^{3+}/\sum Fe$ of the EC basalts reflect the mantle source signature.

In a few samples, alteration is visible as evidenced by the iddingsitization of olivines and elevated loss of ignition (LOI). These samples have $Fe^{3+}/\sum Fe$ values similar to samples without iddingsites from the same locality (Supplementary Fig. 5), suggesting that low-temperature iddingsite alteration of olivine has a negligible effect on the bulk rock $Fe^{3+}/\sum Fe$. The absence of a correlation between $Fe^{3+}/\sum Fe$ and LOI (Supplementary Fig. 5) further indicates that the high bulk rock $Fe^{3+}/\sum Fe$ is not controlled by surface alteration.

Crustal contamination is negligible in EC basalts (*14, 15*), as indicated by the absence of positive Pb and negative Nb-Ta anomalies in trace element patterns (Fig. 1C). In plots of $Fe^{3+}/\sum Fe$ vs. Sr and Nd isotopes (Supplementary Fig. 6), the enriched samples with low $\varepsilon_{Nd(i)}$ and high $^{87}Sr/^{88}Sr_i$ values tend to have lower $Fe^{3+}/\sum Fe$ values, suggesting that crustal contamination (if any) is unlikely responsible for the high $Fe^{3+}/\sum Fe$ values observed in EC basalts.

The presence of olivine and in rare cases pyroxene phenocrysts in the groundmass of EC basalts suggests that magmas have experienced crystal fractionation of olivine and pyroxene. Iron oxides are only found in groundmass in all samples, consistent with the high bulk rock MgO contents of EC basalts (MgO > 6 wt%; Fig. 2D). Crystallization of olivine and pyroxene has a limited effect on the bulk rock $Fe^{3+}/\sum Fe$ (*23-25*). Specifically, a 2% decrease of MgO leads to a 0.01 increase in melt $Fe^{3+}/\sum Fe$ (*24*). This inference is consistent with the lack of a correlation between MgO and $Fe^{3+}/\sum Fe$ ($R^2 = 0.27$) in the investigated EC basalts (Fig. 2D). To eliminate the possible effect of crystal fractionation or crystal accumulation, the $Fe^{3+}/\sum Fe$ data were corrected by adding or subtracting equilibrium olivine until bulk rock reaches $Mg\#_{melt}$=0.72 or 0.63, which corresponds to equilibrium with Fo_{90} or Fo_{85} olivines. The maximum correction for $Fe^{3+}/\sum Fe$ is less than 0.08 (Supplementary Section 2 and Supplementary Fig. 7), which is comparable to the analytical uncertainty.

Since Fe^{3+} is more incompatible than Fe^{2+} during mantle partial melting (*26*), melts are expected to have higher $Fe^{3+}/\sum Fe$ relative to their sources. For example, global MORB and OIB have higher $Fe^{3+}/\sum Fe$ than the normal-mantle value of 0.036 (*2, 4, 18, 27, 28*). However, a recent study observed a constant $Fe^{3+}/\sum Fe$ value over variable degrees of partial melting (*25*). Our partial melting calculation also shows that melting of a normal mantle source can only produce melts with $Fe^{3+}/\sum Fe$ about 0.07 higher at most relative to the source (Supplementary Section 3 and Supplementary Fig. 8).

Magma degassing can cause a variation in $Fe^{3+}/\sum Fe$ (*20*). Hydrogen loss as H_2 may increase $Fe^{3+}/\sum Fe$ in the magma, but direct measurement of degassing volcanoes shows that H_2 is a minor component in degassed species compared to the more abundant oxidized species dominated by H_2O, CO_2 and SO_2 (*29*). While H_2O and CO_2 degassing has negligible effects on the $Fe^{3+}/\sum Fe$ of magma, sulfur degassing could potentially change the redox state of the degassed magma (*2, 30-32*). Degassing of moderately reduced melts can decrease bulk rock $Fe^{3+}/\sum Fe$, with six moles of Fe^{3+} being reduced to Fe^{2+} for every mole of S^{2-} degassed as SO_2 (*20*). In contrast, degassing of oxidized melts can increase bulk rock $Fe^{3+}/\sum Fe$ (*30, 33*), if sulfur in forms of SO_4^{2-} was reduced to SO_2 by oxidizing the Fe^{2+} to Fe^{3+}. Due to the lack of information on the sulfur species in both magmas and gasses during the eurption of the EC basalts, the effect of sulfur degassing on the redox change of the degassed magma is difficult to constrain. Nevertheless, to evaluate the possible oxidizing effect caused by degassing of SO_2 for subaerial volcanoes, we assume that the magma with a total FeO of 12 wt% and $Fe^{3+}/\sum Fe$ of 0.25 has an initial sulfur content of 2500 ppm in forms of sulfate, and experiences 95% degassing to SO_2. This oxidized degassing scenario could elevate the $Fe^{3+}/\sum Fe$ of a degassed magma by 0.1 at most. Therefore, sulfur degassing alone cannot explain the observed high $Fe^{3+}/\sum Fe$ of the EC basalts.

Collectively, although all the above-mentioned shallow processes may have modified the $Fe^{3+}/\sum Fe$ in manners that we are unable to precisely constrain, the well-defined relationships between $Fe^{3+}/\sum Fe$ and key magmatic parameters, such as olivine $\delta^{18}O$ value and V/Sc ratio (Fig. 2B, C), strongly suggest that the parent melts of EC basalts are highly oxidized. Olivine is the first mineral to crystallize from primitive basaltic magma during cooling, and thus geochemical signatures preserved in olivine phenocrysts are less affected by late and post-eruptive processes. Within olivine grains, the rim-core-rim analyses show uniform V, Sc and $\delta^{18}O$ values (Supplementary Fig. 3), precluding the possible diffusion effect between olivine and melt. The V partitioning between olivine and melt is redox-sensitive, with olivine formed in a reduced magma having higher concentrations of V. In contrast, the partitioning of Sc between olivine and melt is redox-insensitive. As such, the V/Sc in olivine phenocrysts records the magma redox state, with lower ratios deviating from the primitive mantle value (V/Sc = 4.9) (*22*) indicating more oxidizing conditions (*34, 35*). The negative correlation between $Fe^{3+}/\sum Fe$ and olivine V/Sc (R^2 = 0.81; Fig. 2C) validates the utility of bulk rock $Fe^{3+}/\sum Fe$ as a redox proxy of primitive magma. In addition, the $Fe^{3+}/\sum Fe$ values are well correlated with a number of elemental and stable isotopic ratios (shown below) that are unaffected by magmatic or post-emplacement processes (Figs. 3 and 4), further supporting that their highly oxidized nature is a source signature.

The nature of high $Fe^{3+}/\sum Fe$ endmember

The EC intraplate basalts are as oxidized as arc basalts with similar ranges in $Fe^{3+}/\sum Fe$; however, they show opposite $Fe^{3+}/\sum Fe$ versus Th/Ba and U/Pb trends (Fig. 3), implying different oxidation mechanisms. The highly oxidized nature of arc basalts is likely caused by the addition of slab-derived oxidizing fluids to the sub-arc mantle wedge source (*36*). A compilation of global arc basalt data shows that the high $Fe^{3+}/\sum Fe$ values are associated with low Th/Ba and U/Pb ratios (Fig. 3). This is a consequence of slab-derived fluid addition, because Ba and Pb are more mobile in fluid than Th and U (*37*). Conversely, the EC intraplate basalts have higher Th/Ba and U/Pb ratios which increase with $Fe^{3+}/\sum Fe$ values (Fig. 3). These correlations suggest that the oxidation of EC intraplate basalts is related to the stagnant Pacific slab that has preferentially lost fluid-mobile elements through dehydration processes during subduction.

Within EC intraplate basalts, high $Fe^{3+}/\sum Fe$ values are coupled with low Hf/Hf*, Ti/Ti*, Zr/Nd, and high CaO/Al_2O_3 (Fig. 4A-D). Carbonated melts are characterized by high CaO/Al_2O_3 and extreme depletion of high field strength elements (HFSEs, such as Zr, Hf, and Ti) relative to

rare earth elements (Fig. 1C) (*38*). The negative correlations of $Fe^{3+}/\sum Fe$ with Hf/Hf*, Ti/Ti* and Zr/Nd, and positive correlation of $Fe^{3+}/\sum Fe$ with CaO/Al_2O_3 thus indicate an essential role of a highly oxidized, carbonated endmember in the petrogenesis of EC basalts.

The Mg and Zn isotopic systematics further support that the carbonated melts may be derived from the subducted carbonated Pacific slab. Nearly all EC basalts exhibit higher $\delta^{66}Zn$ and lower $\delta^{26}Mg$ values compared to those of the primitive mantle or MORB (Fig. 4E, F) (*16, 39*). Given that Mg and Zn isotopes do not substantially fractionate during partial melting (*40, 41*), the high $\delta^{66}Zn$ and low $\delta^{26}Mg$ signatures in EC basalts are best explained as a result of involving recycled carbonates that have distinctively lighter Mg and heavier Zn isotopic compositions ($\delta^{66}Zn$ up to +1.7‰; $\delta^{26}Mg$ down to -5‰; see Supplementary Fig. 9 for a compilation of Mg and Zn isotopic compositions of sedimentary carbonates) in the mantle sources of EC basalts (*16, 39*). High-pressure high-temperature experiments suggest that subducted carbonated oceanic crust partially melts at the MTZ depth (*42*), and produces carbonated melts with high-$\delta^{66}Zn$ and low-$\delta^{26}Mg$ signatures of marine carbonates (*16, 39*). The Pacific plate experienced a prolonged carbonation (*43*) and the altered oceanic crust recovered from the ODP Hole 801C contains ~1 wt% CO_2 on average (*44*). Subsequent low-degree melting of the subducted carbonated oceanic crust at the MTZ would preferentially consume carbonate minerals at the onset of melting to form carbonated melts (*42*). To account for the Zn and Mg isotopic composition of the carbonated melt endmember, mass balance predicts that during low-degree melting of the subducted carbonated oceanic crust, carbonate minerals in forms of dolomite or magnesite contributed as high as 10-20% in the melting reactions (Supplementary section 4 for modelling details and Supplementary Fig. 10). Although it is difficult to make a tight constraint on the carbonate contribution using only Mg and Zn isotopic systematics in EC basalts, the positive $Fe^{3+}/\sum Fe$ versus $\delta^{66}Zn$ trend and negative $Fe^{3+}/\sum Fe$ versus $\delta^{26}Mg$ trend reveal that the recycled carbonates have played an important role in oxidizing the mantle source of EC basalts.

Since low Hf/Hf*, Ti/Ti*, Zr/Nd, and high U/Pb, Th/Ba, CaO/Al_2O_3 are typical characteristics of the HIMU endmember (*5, 45*), the high-$Fe^{3+}/\sum Fe$ endmember of EC basalts may be a highly oxidized HIMU-like mantle endmember, which is related to carbonated melts originated from the stagnant Pacific slab at the MTZ beneath EC. We define this endmember as Highly Oxidized Mantle Endmember (HOME). Consistent with this argument, the compositions of EC Cenozoic intraplate basalts in plots involving $Fe^{3+}/\sum Fe$ point toward the HIMU-type high-$Fe^{3+}/\sum Fe$ (0.85) diamond inclusion (Figs. 4A-D), whose petrogenesis is related to partial melting of carbonated MORB at MTZ (*5*). In addition, the OIB averages also plot along the EC Cenozoic intraplate basalt trends (Figs. 3, and 4A-D), implying that HOME may be widely sampled by global OIB as well (*2*).

Olivine-$\delta^{18}O$ values in EC basalts are also correlated with the above-mentioned bulk rock geochemical indices (Fig. 5). The hypothetical HOME endmember is inferred to have mantle-like to higher olivine-$\delta^{18}O$ values, consistent with its carbonated origin (*46*). The low-$\delta^{18}O$ endmember may be related to the sub-continental lithospheric mantle, which has experienced extensive metasomatism by fluid/melts derived from hydrothermally altered subducted oceanic crust (*47*). Consistent with this inference, the metasomatized mantle xenolith PIC (Phlogopite-Ilmenite-Clinopyroxene) has a light O isotopic composition, located at the low-$\delta^{18}O$ endmember in the trends shown in Figure 5 (*46*). A recent olivine-$\delta^{18}O$ investigations of global kimberlites from different cratons also show that the metasomatized sub-continental lithospheric mantle is an important reservoir of isotopically-light oxygen (*46*). Below we focus on the HOME and discuss how it is produced using experimental results of carbon-iron redox reactions and first-principles simulations (See Supplementary Section 5 for computational details).

HOME produced by carbon-iron redox reaction

Mantle carbon-iron redox reaction can efficiently oxidize the mantle, in which Fe^{2+} is oxidized to Fe^{3+} by the reduction of carbonate to diamond. This reaction can be broken into two steps. First, disproportionation of Fe^{2+} ($3Fe^{2+} \rightarrow Fe^0 + 2Fe^{3+}$) that occurs in the mantle below ~250 km depth (*7, 48*). Second, carbonates in the deep upper mantle can be reduced to diamond by oxidizing metal Fe through a redox reaction of $2Fe^0 + C^{4+} \rightarrow 2Fe^{2+} + C^0$ (*7*). As such, the net reaction involving both carbonate and Fe^{2+} in silicates is: $4Fe^{2+} + C^{4+} \rightarrow 4Fe^{3+} + C^0$, in which C^0 is formed as diamond because of high pressure.

This reaction may be favored in mantle domains where excess amount of carbonate is available, such as slab subduction and accumulation in the upper mantle and/or MTZ at places like BMW beneath EC (Fig. 1B). The subducted Paleo-Pacific slab may have penetrated into the lower mantle or consumed by ambient mantle, but the development of the BMW and slab stagnation in the MTZ since early Cretaceous have acted as a barrier for whole mantle convention (*11, 12*).

Another key for this reaction to occur toward right is to continuously remove the produced C^0 as diamond. To investigate the density difference between diamond and melts, we performed first-principles molecular dynamics (FPMD) simulations based on density functional theory (DFT) to determine the melt-diamond density crossover at mantle depths (See Supplementary Section 5 for computational details). We focused on three types of silicate melts, $Mg_6Ca_6Fe_5Si_{27}Al_{10}Na_3O_{88}$ (dry MORB), $Mg_6Ca_6Fe_5Si_{27}Al_{10}Na_3H_{18}O_{97}$ (MORB with 4.9 wt.% water), and $Mg_6Ca_6Fe_5Si_{27}Al_{10}Na_3C_4O_{96}$ (MORB with 5.3 wt% CO_2) to model the effects of volatiles (Supplementary Table 5 and 6). Our simulations together with previous studies show that diamond is always denser than silicate and carbonated melts at the bottom of upper mantle (~12-14 GPa). Because the density of melt decreases with increasing H_2O and CO_2 contents, the location of silicate/carbonated melt-diamond density crossover could be even deeper if the melt is more volatile-rich (Fig. 6A).

In summary, under the conditions of the lowermost upper mantle and the MTZ where redox reactions between Fe and C occurs, diamond formed through this reaction would sink and be separated from the melts because of its high density. This would prompt the carbon-iron redox reaction toward right, and leave a highly oxidized melt.

Based on above discussion, we propose that the formation of HOME is closely related to the carbonated melts produced by low-degree partial melting of the stagnant carbonated slabs at the MTZ beneath EC. These carbonated melts are expected to have low Hf/Hf*, Ti/Ti*, Zr/Nd, $\delta^{26}Mg$, and high U/Pb, Th/Ba, CaO/Al_2O_3, $\delta^{66}Zn$, characteristics of the HOME of EC basalts. Growth and separation of diamond from these carbonated melts as a result of the iron-carbon redox freezing reaction would have enriched the melts with Fe^{3+} (Fig. 6C). This mechanism is consistent with the traditional view that the HIMU endmember is partial melt of recycled ancient carbonated MORB (*5, 49, 50*). The highly oxidized carbonated melts could also react with and metasomatize the asthenospheric peridotite in the BMW. The outcome of this carbonated melt-peridotite interaction is twofold. First, the interaction progressively oxidizes the Fe^{2+} in peridotites to Fe^{3+}, and reduces C^{4+} to form diamonds that are subsequently removed from the carbonated melt because of density difference. Second, metasomatism by carbonated melt leads to the low Hf/Hf*, Ti/Ti*, Zr/Nd, $\delta^{26}Mg$, and high U/Pb, Th/Ba, CaO/Al_2O_3, $\delta^{66}Zn$ signatures in the metasomatized peridotites. We envision that there is excess amount of CO_2 in the melt, so that the metasomatized peridotite can have a high $Fe^{3+}/\sum Fe$, and the remaining CO_2 will lower the solidus of the metasomatized peridotites (Fig. 6B), leading to low-degree partial melting that produces melts inherited the HOME signature (Fig. 6C). This mechanism is consistent with the alternative

inference that the HIMU endmember is low-degree partial melt of carbonate-metasomatized peridotite (*45*).

Collectively, the uniquely high $Fe^{3+}/\sum Fe$ characteristics of EC basalts require that their mantle source(s) must be deep in the mantle (> 300 km), within the pressure range that allows redox freezing reaction to happen, consistent with the most recent inference that the HIMU mantle source resides in the MTZ (*5, 49*).

Interestingly, averages of OIB form trends overlapping with the EC Cenozoic basalt trend, pointing toward the hypothetical HOME (Figs. 3, and 4A-D). The HIMU-flavored basalts in general have higher $Fe^{3+}/\sum Fe$ than MORB (*2*), though not as high as those observed in EC intraplate basalts. The formation of HOME requires excess amounts of carbonates to oxidize all metal Fe in the mantle domains produced by Fe^{2+} disproportionation before converting Fe^{2+} to Fe^{3+}. The unique geological setting of the BMW beneath EC makes it possible. The long-term subduction and stagnancy of Pacific slab at the MTZ since early Cretaceous not only provides vast amounts of carbonates, but also blocks mantle flow from the lower mantle that may be an infinite source for reduced metal Fe. It remains to be explored whether HOME is a common feature for all HIMU-type basalts, or it is only associated to and more prominent in specific geological settings, for example, the BMW developed at circum-Pacific subduction zones.

Deep carbon storage

The redox freezing reaction and the subsequent melt-diamond separation would have resulted in the substantial storage of carbon within the deep mantle. The redox reaction of $4Fe^{2+} + C^{4+} \rightarrow 4Fe^{3+} + C^0$ can be used to estimate the overall quantity of carbon required for oxidizing the EC basalts and subsequently sequestering it from the global carbon cycle. The area of EC Cenozoic basalt can be determined by overlaying the distribution information of Cenozoic basalts on high-precision geomorphologic map, where the distribution information can be extracted by pixel from the geological map of eastern China using digital-image processing program (*51*). The total area of EC Cenozoic basalts was estimated at about 79,000 km^2 (*51*). Assuming the layer thickness of the EC basalts is 10 km, 2400 Gt (gigaton) of carbon would be stored at the BMW to elevate the $Fe^{3+}/\sum Fe$ of EC basalts from a MORB-like value of 0.14 to an average value of 0.35 for the studied EC basalts (< 50 Ma) (Supplementary Section 6 for modelling details and Supplementary Fig. 11), which is ~four times the amount of pre-industrial atmospheric carbon budget (590 Gt). The estimate entails several uncertainties. For instance, the total volume of Cenozoic intraplate basalts can vary substantially as its thickness is poorly constrained in many locations, and the measured $Fe^{3+}/\sum Fe$ do not represent the actual value of the parent melt considering the uncertainties from degassing and crystal fractionation. In addition, it is likely that the $Fe^{3+}/\sum Fe$ of melts could be decreased due to the reverse redox reaction ($4Fe^{3+} + C^0 \rightarrow 4Fe^{2+} + C^{4+}$) as the melts ascend and percolate across the redox melting frontline (~250 km) (*52, 53*), and mix with the lithospheric mantle-derived melts. Nevertheless, we argue for a link between oxidized intraplate basalts and deep carbon storage, both of which may form from subducted slab stagnant at MTZ. Seismic images of the circum-Pacific reveal that the uppermost lower mantle (660-1000km) is an important reservoir for the subducted slabs, forming BMW around the majority of the circum-Pacific (*54*). Therefore, the formation of HOME may not be restricted to BMW beneath eastern China. The possible climate effect of the deep carbon storage associated with the formation of the HOME in the geological history needs further investigations.

MATERIALS AND METHODS

Wet chemistry $Fe^{3+}/\Sigma Fe$ analysis

$Fe^{3+}/\Sigma Fe$ ratios were measured using redox titration with a potassium dichromate ($K_2Cr_2O_7$) solution at the Element Geochemistry Laboratory of the China University of Geosciences, Beijing (*55*). 100 mg of sample powders were mixed with 5 mL concentrated hydrofluoric acid (HF) and 10 mL 1:1 Milli-Q water: sulfuric acid (H_2SO_4) in PTFE crucibles with lid. The mixtures were heated on a hotplate until they reached boiling temperature. After heating for another 10 minutes, the mixtures were complexed and buffered by 25 mL boric acid (H_3BO_3) and 150 mL Milli-Q water at room temperature. 15 mL 3:7 H_3PO_4-H_2SO_4 mixture was added into the solutions before titration. Ferrous Fe was then titrated by 0.01 mol/L $K_2Cr_2O_7$ with sodium diphenylamine sulfonate ($C_{12}H_{10}NSO_3Na$) as the indicator. We used the certified FeO value (FeO = 7.60%) of rock standard GSR-3 to calibrate the potassium dichromate concentration. The $Fe^{3+}/\Sigma Fe$ was calculated as $(FeO_{total} - FeO)/FeO_{total}$. Five rock reference materials including BCR-2, BHVO-2, GSR-1, GSR-2 and GSR-3 were processed together with samples as unknowns. Their measured FeO contents agree with their reported certified values (*55, 56*), with analytical uncertainties within ± 10% in $Fe^{3+}/\Sigma Fe$ (Supplementary Table 2). The results of EC Cenozoic intraplate basalts are shown in Supplementary Table 1. Repeated analyses of FeO for a selected set of samples show in good agreement between duplicates within ±10% (Supplementary Table 1).

Mössbauer spectra $Fe^{3+}/\Sigma Fe$ analysis

In order to verify the $Fe^{3+}/\Sigma Fe$ measured using wet-chemistry, we performed Mössbauer spectroscopy to determine the $Fe^{3+}/\Sigma Fe$ of a subset of samples that cover the entire range of $Fe^{3+}/\Sigma Fe$. The Mössbauer spectra (MBS) were collected and processed to identify Fe species with different oxidation states. The MBSs were obtained using a Mössbauer spectrometer (MS-65, Science Engineering & Education Co, USA) with a high-velocity resolution (registered in 1024 channels) at ~12 K (cooled down by liquid helium, but the system was not able to reach 4.2 K due to the low power of the compressor) coupled with a SHI-850 cryogenic system from Janis Research Co., Inc. (Wilmington, MA) at the Institute of Geochemistry, Chinese Academy of Sciences (IGCAS). ^{57}Co in the Rh matrix provided ~14.4 eV gamma rays. Each sample of 20 to 40 mg was loaded in the Cu sample holder with a 1.0-cm diameter window and a thickness as large as ~0.3 cm to accommodate any large-sized sample. The holder was entirely sealed with Kapton tape. The precise weight of each sample is calculated to match the ideal absorber thickness, which optimizes the signal-to-noise ratio (*57*).

All measurements were performed in a velocity range of ± 10 mm/s to ensure that any hyperfine split pattern (e.g., sextets) from magnetically ordered Fe-bearing phases was detected. The Mössbauer spectrum reflects the nature and strength of the hyperfine interactions, whose key parameters consist of the isomer shift (IS), quadrupole splitting (QS or ε), and magnetic field (T). The velocity zero is defined as the center of the α-Fe calibration spectrum (e.g., at ~295 K). The isomer shift (IS) is the velocity shift of the samples relative to the source and is expressed relative to the α-iron calibration spectrum, which can be used to identify the electronic structure of the atom and then give its valence and spinning state. The electric quadrupole splitting parameter (QS or ε) is a measure of the spatial distribution of electrons around the ^{57}Fe nucleus and is influenced by both asymmetry of valence electrons and longer-range contributions from the entire mineral lattice (*58*). The magnetic field (T) is used to measure the interaction between the nuclear magnetic moment and the net effective magnetic field on the nucleus. The collection time in the cryogenic measurements is approximately 3-4 days to improve precision. During cryogenic measurements, the temperature was kept below11 K during data acquisition, which was detected at the He gas outflow port and on the sample holder mount. Data were collected over 512 channels, which on folding resulted in 256 channels. The raw data were folded to eliminate the geometric effect and then fitted using the least-square method with one or more appropriate sets of Lorentzian lines by 4.0Pre of the MossWinn program (http://www.mosswinn.com). The main fitting parameters

include isomer shift, magnetic field, and quadrupole splitting. The std and chi square (goodness of fit, χ^2) of all the parameters are calculated by 100 Monte Carlo iterations on MossWinn 4.0.

The relative areas of the individual components in the MBS can be considered as representing the amounts of Fe in the respective phases to a good approximation because the resonant fractions of the individual phases present in the samples do not differ largely (*59*). In this study, Fe^{2+}/Fe^{3+} was assessed using MBS collected at ~12 K. In the 12 K spectra, different spectral components of samples were resolved: (1) an Fe^{III} quadrupole doublet (e.g., 10FS10) or an Fe^{III} quadrupole doublet and an Fe^{III} sextet (e.g., 08LHS02); (2) an Fe^{II} quadrupole doublet. All the parameters (e.g., IS) of these spectral components are shown in Supplementary Table 3.

The Mössbauer spectra $Fe^{3+}/\Sigma Fe$ data agree with the wet-chemistry $Fe^{3+}/\Sigma Fe$ within ±10% (Fig. 2A in the main text), further confirming the accuracy of wet-chemistry $Fe^{3+}/\Sigma Fe$ measurement of EC basalts.

In situ SIMS oxygen isotope analysis

We measured oxygen isotopic compositions of olivines at the Institute of Geology and Geophysics, Chinese Academy of Sciences (IGGCAS), Beijing, China. First, we drilled out the selected portions of the thin sections and mounted them together with the oxygen isotope reference material San Carlos olivine in epoxy resin. Then sample mounts were polished and gold-coated. Oxygen isotopic ratios of olivine were analyzed using CAMECA IMS-1280 multi-collector ion probe. The Cs^+ primary beam was accelerated at 10 kV with an intensity of ca. 2 nA. The spot is approximately 20 μm in diameter (10 μm beam diameter +10 μm raster). An electron gun was used to compensate for sample charging during the analysis. Secondary ions were extracted at a -10kV potential. Oxygen isotopes were measured in multi-collector mode with two off-axis Faraday cups. Each analysis consisted of 20 cycles with 4 s counting time. We analyzed the reference material San Carlos olivine after analyzing every four unknown samples in the experiment to monitor analytical precision and calibrate instrumental mass fractionation. The average $\delta^{18}O$ value for San Carlos olivine is 5.23 ‰, with an external reproducibility (2SD) of 0.38 ‰ in this study, which is similar to the reported certified value of 5.3 ‰ (*60*). Previous studies have demonstrated negligible matrix effect for olivine with Fo numbers > 70 (*61*). SIMS oxygen isotope analysis on olivine with Fo number < 70 has significant instrumental mass fractionation (*61-65*). Therefore, only olivine grains with Fo number > 70 were selected for oxygen isotope analysis.

Laser ablation inductively coupled plasma mass spectrometry (LA-ICP-MS)

After SIMS analyses, the gold coating was removed. We determined the elemental compositions of olivine using a GeolasHD 193 nm ArF excimer LA system (Coherent; Göttingen, Germany) coupled to an Element XR sector field (SF)–ICP–MS (Thermo Fisher Scientific; Bremen, Germany) at the Institute of Geology and Geophysics, Chinese Academy of Sciences (IGGCAS), Beijing, China. Helium was used as the carrier gas and mixed with Ar gas before being transported to the plasma torch. Olivines were analyzed at laser repetition of 5 Hz, energy density of 3 J/cm^2, and spot size of 32 μm. The locations of the laser spots were selected based on binocular microscopic and BSE image examination to avoid any cracks and inclusions. Each spot was ablated for 40 seconds for ICP-MS measurement after 10 seconds of blank gas measurement, followed by 10 seconds of washout. Possible surface contamination was removed in a pre-ablation step with three laser pulses before analyzing. ARM-3 reference glass were used for the instrument- and time-dependent fractionations of Fe/Mg ratios and all minor–trace elements (*66*). Olivine standard RM MongOLSh11-2 and XEN were measured as unknown for data quality control. RM MongOLSh11-2 has average concentrations of 5.99 μg/g (2SD=0.39) for V and 3.7 μg/g (2SD=0.42) for Sc, and

XEN has average concentrations of 2.09 μg/g (2SD=0.26) and 2.1 μg/g (2SD=0.4) for V and Sc, in agreement with the reported certified values (*67, 68*). Each set of standard samples, including ARM-3, GOR132-G, MongOLSh11-2 and XEN, was analyzed once every 10 unknown samples were interspersed.

References

1. D. J. Frost, C. A. McCammon, The Redox State of Earth's Mantle. *Annu. Rev. Earth Planet. Sci.* **36**, 389-420 (2008).
2. Y. Moussallam, M.-A. Longpré, C. McCammon, A. Gomez-Ulla, E. F. Rose-Koga, B. Scaillet, N. Peters, E. Gennaro, R. Paris, C. Oppenheimer, Mantle plumes are oxidised. *Earth Planet. Sci. Lett.* **527**, 115798 (2019).
3. Y. S. He, X. Meng, S. Ke, H. Wu, C. Zhu, F.-Z. Teng, J. Hoefs, J. Huang, W. Yang, L. Xu, Z. Hou, Z.-Y. Ren, S. Li, A nephelinitic component with unusual δ^{56}Fe in Cenozoic basalts from eastern China and its implications for deep oxygen cycle. *Earth Planet. Sci. Lett.* **512**, 175-183 (2019).
4. R. W. Nicklas, R. K. M. Hahn, L. N. Willhite, M. G. Jackson, V. Zanon, R. Arevalo, J. M. D. Day, Oxidized mantle sources of HIMU- and EM-type Ocean Island Basalts. *Chem. Geol.* **602**, 120901 (2022).
5. S. C. Huang, O. Tschauner, S. Y. Yang, M. Humayun, W. J. Liu, S. N. G. Corder, H. A. Bechtel, J. Tischler, HIMU geochemical signature originating from the transition zone. *Earth Planet. Sci. Lett.* **542**, 116323 (2020).
6. E. S. Kiseeva, D. M. Vasiukov, B. J. Wood, C. McCammon, T. Stachel, M. Bykov, E. Bykova, A. Chumakov, V. Cerantola, J. W. Harris, L. Dubrovinsky, Oxidized iron in garnets from the mantle transition zone. *Nat. Geosci.* **11**, 144-147 (2018).
7. A. Rohrbach, M. W. Schmidt, Redox freezing and melting in the Earth's deep mantle resulting from carbon-iron redox coupling. *Nature* **472**, 209-212 (2011).
8. R. B. Tao, Y. W. Fei, Recycled calcium carbonate is an efficient oxidation agent under deep upper mantle conditions. *Commun. Earth Environ.* **2**, 1-8 (2021).
9. J. L. Huang, D. P. Zhao, High-resolution mantle tomography of China and surrounding regions. *J. Geophys. Res.* **111**, B09305 (2006).
10. E. Ohtani, D. Zhao, The role of water in the deep upper mantle and transition zone: dehydration of stagnant slabs and its effects on the big mantle wedge. *Russ. Geol. Geophys.* **50**, 1073-1078 (2009).
11. S. G. Li, Y. Wang, Formation time of the big mantle wedge beneath eastern China and a new lithospheric thinning mechanism of the North China craton-Geodynamic effects of deep recycled carbon. *Sci. China Earth Sci.* **61**, 853-868 (2018).
12. Q. Ma, Y.-G. Xu, Magmatic perspective on subduction of Paleo-Pacific plate and initiation of big mantle wedge in East Asia. *Earth Sci. Rev.* **213**, 103473 (2021).
13. Y. Xu, H. Li, L. Hong, L. Ma, Q. Ma, M. Sun, Generation of Cenozoic intraplate basalts in the big mantle wedge under eastern Asia. *Sci. China Earth Sci.* **61**, 869-886 (2018).
14. R. Xu, Y. Liu, X.-C. Wang, S. F. Foley, Y. Zhang, H. Yuan, Generation of continental intraplate alkali basalts and implications for deep carbon cycle. *Earth Sci. Rev.* **201**, 103073 (2020).
15. G. Zeng, L. H. Chen, X. S. Xu, S. Y. Jiang, A. W. Hofmann, Carbonated mantle sources for Cenozoic intra-plate alkaline basalts in Shandong, North China. *Chem. Geol.* **273**, 35-45 (2010).
16. S. G. Li, W. Yang, S. Ke, X. Meng, H. Tian, L. J. Xu, Y. S. He, J. Huang, X. C. Wang, Q. Xia, W. D. Sun, X. Y. Yang, Z. Y. Ren, H. Q. Wei, Y. S. Liu, F. C. Meng, J. Yan, Deep carbon cycles constrained by a large-scale mantle Mg isotope anomaly in eastern China.

Nat. Sci. Rev. **4**, 111-120 (2017).
17. Y. Liu, S. Gao, P. B. Kelemen, W. Xu, Recycled crust controls contrasting source compositions of Mesozoic and Cenozoic basalts in the North China Craton. *Geochim Cosmochim Ac* **72**, 2349-2376 (2008).
18. H. L. Zhang, E. Cottrell, P. A. Solheid, K. A. Kelley, M. M. Hirschmann, Determination of $Fe^{3+}/\Sigma Fe$ of XANES basaltic glass standards by Mössbauer spectroscopy and its application to the oxidation state of iron in MORB. *Chem. Geol.* **479**, 166-175 (2018).
19. M. Brounce, E. Stolper, J. Eiler, The mantle source of basalts from Reunion Island is not more oxidized than the MORB source mantle. *Contrib. to Mineral. Petrol.* **177**, 7 (2021).
20. Y. Moussallam, C. Oppenheimer, B. Scaillet, F. Gaillard, P. Kyle, N. Peters, M. Hartley, K. Berlo, A. Donovan, Tracking the changing oxidation state of Erebus magmas, from mantle to surface, driven by magma ascent and degassing. *Earth Planet. Sci. Lett.* **393**, 200-209 (2014).
21. D. Mattey, D. Lowry, C. Macpherson, Oxygen isotope composition of mantle peridotite. *Earth Planet. Sci. Lett.* **128**, 231-241 (1994).
22. C. T. A. Lee, W. P. Leeman, D. Canil, Z. X. A. Li, Similar V/Sc systematics in MORB and arc basalts: Implications for the oxygen fugacities of their mantle source regions. *J. Petrol.* **46**, 2313-2336 (2005).
23. K. A. Kelley, E. Cottrell, The influence of magmatic differentiation on the oxidation state of Fe in a basaltic arc magma. *Earth Planet. Sci. Lett.* **329**, 109-121 (2012).
24. O. Shorttle, Y. Moussallam, M. E. Hartley, J. Maclennan, M. Edmonds, B. J. Murton, Fe-XANES analyses of Reykjanes Ridge basalts: Implications for oceanic crust's role in the solid Earth oxygen cycle. *Earth Planet. Sci. Lett.* **427**, 272-285 (2015).
25. Y. Moussallam, G. Georgeais, E. F. Rose-Koga, K. T. Koga, M. E. Hartley, B. Scaillet, C. Oppenheimer, N. Peters, CO_2-Undersaturated Melt Inclusions From the South West Indian Ridge Record Surprisingly Uniform Redox Conditions. *Geochem. Geophys. Geosyst.* **24**, e2023GC011235 (2023).
26. G. A. Gaetani, The behavior of $Fe^{3+}/\sum Fe$ during partial melting of spinel lherzolite. *Geochim Cosmochim Ac* **185**, 64-77 (2016).
27. E. Cottrell, S. K. Birner, M. Brounce, F. A. Davis, L. E. Waters, K. A. Kelley, "*Oxygen Fugacity Across Tectonic Settings"* in *Magma Redox Geochemistry,* R. Moretti, D. R. Neuville, Eds (Wiley, 2021), pp. 33-61.
28. D. Canil, H. S. Oneill, D. G. Pearson, R. L. Rudnick, W. F. Mcdonough, D. A. Carswell, Ferric Iron in Peridotites and Mantle Oxidation-States. *Earth Planet. Sci. Lett.* **123**, 205-220 (1994).
29. Y. Moussallam, C. Oppenheimer, A. Aiuppa, G. Giudice, M. Moussallam, P. Kyle, Hydrogen emissions from Erebus volcano, Antarctica. *Bull. Volcanol.* **74**, 2109-2120 (2012).
30. F. Gaillard, B. Scaillet, M. Pichavant, G. Iacono-Marziano, The redox geodynamics linking basalts and their mantle sources through space and time. *Chem. Geol.* **418**, 217-233 (2015).
31. R. Moretti, D. R. Neuville, Eds. *Magma Redox Geochemistry* (American Geophysical Union, Wiley 2022).
32. Y. Moussallam, M. Edmonds, B. Scaillet, N. Peters, E. Gennaro, I. Sides, C. Oppenheimer, The impact of degassing on the oxidation state of basaltic magmas: A case study of Kīlauea volcano. *Earth Planet. Sci. Lett.* **450**, 317-325 (2016).
33. S. Ding, T. Plank, P. J. Wallace, D. J. Rasmussen, Sulfur_X: A Model of Sulfur Degassing During Magma Ascent. *Geochem. Geophys. Geosyst.* **24**, e2022GC010552 (2023).
34. D. Canil, Vanadium partitioning and the oxidation state of Archaean komatiite magmas. *Nature* **389**, 842-845 (1997).

35. S. F. Foley, D. Prelevic, T. Rehfeldt, D. E. Jacob, Minor and trace elements in olivines as probes into early igneous and mantle melting processes. *Earth Planet. Sci. Lett.* **363**, 181-191 (2013).
36. K. A. Kelley, E. Cottrell, Water and the oxidation state of subduction zone magmas. *Science* **325**, 605-607 (2009).
37. T. Kogiso, Y. Tatsumi, S. Nakano, Trace element transport during dehydration processes in the subducted oceanic crust: 1. Experiments and implications for the origin of ocean island basalts. *Earth Planet. Sci. Lett.* **148**, 193-205 (1997).
38. M. J. Walter, G. P. Bulanova, L. S. Armstrong, S. Keshav, J. D. Blundy, G. Gudfinnsson, O. T. Lord, A. R. Lennie, S. M. Clark, C. B. Smith, L. Gobbo, Primary carbonatite melt from deeply subducted oceanic crust. *Nature* **454**, 622-625 (2008).
39. S. A. Liu, Z. Z. Wang, S. G. Li, J. Huang, W. Yang, Zinc isotope evidence for a large-scale carbonated mantle beneath eastern China. *Earth Planet. Sci. Lett.* **444**, 169-178 (2016).
40. F. Moynier, D. Vance, T. Fujii, P. Savage, The Isotope Geochemistry of Zinc and Copper. *Rev. Miner. Geochem.* **82**, 543-600 (2017).
41. F. Teng, Z., Magnesium Isotope Geochemistry. *Rev. Mineral. Geochem.* **82**, 219-287 (2017).
42. A. R. Thomson, M. J. Walter, S. C. Kohn, R. A. Brooker, Slab melting as a barrier to deep carbon subduction. *Nature* **529**, 76-79 (2016).
43. M. A. Kendrick, J. X. Zhao, Y. X. Feng, Early accretion and prolonged carbonation of the Pacific Ocean's oldest crust. *Geology* **50**, 1270-1275 (2022).
44. J. C. Alt, D. A. H. Teagle, Hydrothermal alteration of upper oceanic crust formed at a fast-spreading ridge: mineral, chemical, and isotopic evidence from ODP Site 801. *Chem. Geol.* **201**, 191-211 (2003).
45. Y. Weiss, C. Class, S. L. Goldstein, T. Hanyu, Key new pieces of the HIMU puzzle from olivines and diamond inclusions. *Nature* **537**, 666-670 (2016).
46. J. Y. Xu, A. Giuliani, Q. L. Li, K. Lu, J. C. Melgarejo, W. L. Griffin, Light oxygen isotopes in mantle-derived magmas reflect assimilation of sub-continental lithospheric mantle material. *Nat. Commun.* **12**, 6295 (2021).
47. X. C. Wang, S. A. Wilde, Q. L. Li, Y. N. Yang, Continental flood basalts derived from the hydrous mantle transition zone. *Nat. Commun.* **6**, 7700 (2015).
48. A. Rohrbach, C. Ballhaus, U. Golla-Schindler, P. Ulmer, V. S. Kamenetsky, D. V. Kuzmin, Metal saturation in the upper mantle. *Nature* **449**, 456-458 (2007).
49. S. E. Mazza, E. Gazel, M. Bizimis, R. Moucha, P. Beguelin, E. A. Johnson, R. J. McAleer, A. V. Sobolev, Sampling the volatile-rich transition zone beneath Bermuda. *Nature* **569**, 398-403 (2019).
50. P. R. Castillo, The recycling ofmarine carbonates and sources of HIMU and FOZO ocean island basalts. *Lithos* **216**, 254-263 (2015).
51. X. Y. Chen, L. H. Chen, Y. Chen, G. Zeng, J. Q. Liu, Distribution Summary of Cenozoic Basalts in Central and Eastern China. *Geological Journal of China Universities* **20**, 507-519 (2014).
52. V. Stagno, D. O. Ojwang, C. A. McCammon, D. J. Frost, The oxidation state of the mantle and the extraction of carbon from Earth's interior. *Nature* **493**, 84-88 (2013).
53. S. F. Foley, "*Redox Melting in the Mantle"* in *Magma Redox Geochemistry,* R. Moretti, D. R. Neuville, Eds (Wiley, 2021), pp. 93-113.
54. Y. Fukao, M. Obayashi, Subducted slabs stagnant above, penetrating through, and trapped below the 660 km discontinuity. *J Geophys Res-Sol Ea* **118**, 5920-5938 (2013).
55. M. Yin, J. X. Li, Eds. *Analysis of Rock and Minerals* (Geological Publishing House, Beijing 2011), vol. 2, pp. 1–862 (in Chinese).
56. P. A. Sossi, J. D. Foden, G. P. Halverson, Redox-controlled iron isotope fractionation

during magmatic differentiation: an example from the Red Hill intrusion, S. Tasmania. *Contrib. to Mineral. Petrol.* **164**, 757-772 (2012).
57. A. Kumar, M. R. Singh, P. R. Sarma, K. C. Tripathi, Optimized Thickness of Diffusive Mossbauer Absorbers. *J. Phys. D. Appl. Phys.* **22**, 465-466 (1989).
58. A. Thompson, D. G. Rancourt, O. A. Chadwick, J. Chorover, Iron solid-phase differentiation along a redox gradient in basaltic soils. *Geochim Cosmochim Ac* **75**, 119-133 (2011).
59. T. Mansfeldt, S. Schuth, W. Hausler, F. E. Wagner, S. Kaufhold, M. Overesch, Iron oxide mineralogy and stable iron isotope composition in a Gleysol with petrogleyic properties. *J. Soil Sedim.* **12**, 97-114 (2012).
60. J. M. Eiler, C. Graham, J. W. Valley, SIMS analysis of oxygen isotopes: matrix effects in complex minerals and glasses. *Chem. Geol.* **138**, 221-244 (1997).
61. F. Guo, J. T. Guo, C. Y. Wang, W. M. Fan, C. W. Li, L. Zhao, H. X. Li, J. Y. Li, Formation of mafic magmas through lower crustal AFC processes - An example from the Jinan gabbroic intrusion in the North China Block. *Lithos* **179**, 157-174 (2013).
62. J. Eiler, E. M. Stolper, M. C. McCanta, Intra- and Intercrystalline Oxygen Isotope Variations in Minerals from Basalts and Peridotites. *J. Petrol.* **52**, 1393-1413 (2011).
63. N. T. Kita, T. Ushikubo, B. Fu, M. J. Spicuzza, J. W. Valley, Analytical developments on oxygen three isotope analyses using a new generation ion microprobe IMS-1280. *Lunar and Planetary Science XXXVIII (1981)*, (2007).
64. I. Bindeman, A. Gurenko, O. Sigmarsson, M. Chaussidon, Oxygen isotope heterogeneity and disequilibria of olivine crystals in large volume Holocene basalts from Iceland: Evidence for magmatic digestion and erosion of Pleistocene hyaloclastites. *Geochim Cosmochim Ac* **72**, 4397-4420 (2008).
65. A. A. Gurenko, I. N. Bindeman, M. Chaussidon, Oxygen isotope heterogeneity of the mantle beneath the Canary Islands: insights from olivine phenocrysts. *Contrib. to Mineral. Petrol.* **162**, 349-363 (2011).
66. S. T. Wu, G. Worner, K. P. Jochum, B. Stoll, K. Simon, A. Kronz, The Preparation and Preliminary Characterisation of Three Synthetic Andesite Reference Glass Materials (ARM-1, ARM-2, ARM-3) for In Situ Microanalysis. *Geostand. Geoanal. Res.* **43**, 567-584 (2019).
67. V. G. Batanova, J. M. Thompson, L. V. Danyushevsky, M. V. Portnyagin, D. Garbe-Schonberg, E. Hauri, J. I. Kimura, Q. Chang, R. Senda, K. Goemann, C. Chauvel, S. Campillo, D. A. Ionov, A. V. Sobolev, New Olivine Reference Material for In Situ Microanalysis. *Geostand. Geoanal. Res.* **43**, 453-473 (2019).
68. S. T. Wu, Y. D. Wu, Y. H. Yang, H. Wang, C. Huang, L. W. Xie, J. H. Yang, Simultaneous Quantification of Forsterite Content and Minor-Trace Elements in Olivine by LA-ICP-MS and Geological Applications in Emeishan Large Igneous Province. *Minerals-Basel* **10**, 634 (2020).
69. W. F. McDonough, S. s. Sun, The composition of the Earth. *Chem. Geol.* **120**, 223-253 (1995).
70. R. L. Rudnick, S. Gao, "*Composition of the Continental Crust"* in *Treatise on Geochemistry,* H. D. Holland, K. K. Turekian, Eds (Pergamon, 2003), vol. 3, pp. 1–64.
71. Y. Weiss, W. L. Griffin, D. R. Bell, O. Navon, High-Mg carbonatitic melts in diamonds, kimberlites and the sub-continental lithosphere. *Earth Planet. Sci. Lett.* **309**, 337-347 (2011).
72. K. Hoernle, G. Tilton, M. J. Le Bas, S. Duggen, D. Garbe-Schönberg, Geochemistry of oceanic carbonatites compared with continental carbonatites: mantle recycling of oceanic crustal carbonate. *Contrib. Mineral. Petrol.* **142**, 520-542 (2002).
73. J. W. Valley, M. J. Spicuzza, T. Ushikubo, Correlated $\delta^{18}O$ and [Ti] in lunar zircons: a

terrestrial perspective for magma temperatures and water content on the Moon. *Contrib. Miner. Petrol.* **167**, 956 (2014).
74. A. Fitzpayne, A. Giuliani, J. Hergt, D. Phillips, P. Janney, New geochemical constraints on the origins of MARID and PIC rocks: Implications for mantle metasomatism and mantle-derived potassic magmatism. *Lithos* **318**, 478-493 (2018).
75. M. Massuyeau, X. Ritter, C. Sanchez-Valle, A density model for high-pressure carbonate-rich melts applied to carbonatitic magmatism in the upper mantle. *Chem. Geol.* **622**, 121275 (2022).
76. R. Dasgupta, Ingassing, Storage, and Outgassing of Terrestrial Carbon through Geologic Time. *Rev. Miner. Geochem.* **75**, 183-229 (2013).
77. Z. Z. Wang, S. A. Liu, Evolution of Intraplate Alkaline to Tholeiitic Basalts via Interaction Between Carbonated Melt and Lithospheric Mantle. *J. Petrol.* **62**, 1-25 (2021).
78. S. P. Qian, Z. Y. Ren, L. Zhang, L. B. Hong, J. Q. Liu, Chemical and Pb isotope composition of olivine-hosted melt inclusions from the Hannuoba basalts, North China Craton: Implications for petrogenesis and mantle source. *Chem. Geol.* **401**, 111-125 (2015).
79. G. Zeng, L. H. Chen, A. W. Hofmann, X. J. Wang, J. Q. Liu, X. Yu, L. W. Xie, Nephelinites in eastern China originating from the mantle transition zone. *Chem. Geol.* **576**, 120276 (2021).
80. J. Huang, S.-G. Li, Y. Xiao, S. Ke, W.-Y. Li, Y. Tian, Origin of low δ^{26}Mg Cenozoic basalts from South China Block and their geodynamic implications. *Geochim Cosmochim Ac* **164**, 298-317 (2015).
81. F. C. Meng, T. F. Li, H. M. Xue, F. L. Liu, Z. Q. Xu, Two serials of basic magmas from different mantle sources of Late Cretaceous in east Shandong province, China: a comparative study on basalts from Zhucheng and Jiaozhou. *Acta Petrologica Sinica* **22**, 1644-1656 (in Chinese with English abstract) (2006).
82. J. Yang, Petrological and Geochemical studies of the Cenozoic Basalts and Hosted Peridotite Xenoliths in Zhejiang and Fujian Provinces Ph.D. *China University of Geosciences (Beijing)*, (2015).
83. C. Q. Sun, J. Q. Liu, B. Xu, H. T. You, First radiocarbon dating of a Holocene eruption of the Datong volcanic field, eastern China. *J. Volcanol. Geotherm. Res.* **384**, 275-279 (2019).
84. H. Zhao, Z. Liu, C. M. Wang, S. H. Li, Luminescence dating of volcanic eruptions in Datong, northern China. *Quat Geochronol* **30**, 357-362 (2015).
85. D. Luo, L. H. Chen, G. Zeng, Genesis of intra-continental strongly alkaline volcanic rocks: A case study of Dashan neohelinites in Wudi, Shandong Province, North China. *Acta Petrologica Sinica* **25**, 311-319 (in Chinese with English abstract) (2009).
86. S. Z. Sheng, S. J. Wang, X. M. Yang, L. H. Chen, G. Zeng, Y. Xiao, J. Shen, X. H. Dong, Y. W. Lv, Sulfide Dissolution on the Nickel Isotopic Composition of Basaltic Rocks. J. Geophys. *Res. Solid Earth* **127**, e2022JB024555 (2022).
87. Z. Z. Wang, S. A. Liu, L. H. Chen, S. G. Li, G. Zeng, Compositional transition in natural alkaline lavas through silica-undersaturated melt–lithosphere interaction. *Geology* **46**, 771-774 (2018).
88. E. Cottrell, K. A. Kelley, The oxidation state of Fe in MORB glasses and the oxygen fugacity of the upper mantle. *Earth Planet. Sci. Lett.* **305**, 270-282 (2011).
89. P. A. Sossi, O. Nebel, J. Foden, Iron isotope systematics in planetary reservoirs. *Earth Planet. Sci. Lett.* **452**, 295-308 (2016).
90. P. L. Roeder, R. F. Emslie, Olivine-Liquid Equilibrium. *Contrib. to Mineral. Petrol.* **29**, 275–289 (1970).
91. A. D. T. Goode, Oxidation of natural olivines. *Nature* **248**, 500-501 (1974).

92. H. M. Williams, M. Bizimis, Iron isotope tracing of mantle heterogeneity within the source regions of oceanic basalts. *Earth Planet. Sci. Lett.* **404**, 396-407 (2014).
93. M. J. Walter, Melting of garnet peridotite and the origin of komatiite and depleted lithosphere. *J. Petrol.* **39**, 29-60 (1998).
94. J. Wang, F. Huang, X. Xiong, E. Takahashi, "*Partition Coefficients of Fe^{3+} and Fe^{2+} between Mantle Minerals and Melts: Implications for Redox Variations during Mantle Melting*" (AGU Fall Meeting 2021, New Orleans, LA, 2021).
95. R. Dasgupta, M. M. Hirschmann, The deep carbon cycle and melting in Earth's interior. *Earth Planet. Sci. Lett.* **298**, 1-13 (2010).
96. B. B. Karki, First-principles computation of mantle materials in crystalline and amorphous phases. *Phys. Earth Planet.* **240**, 43-69 (2015).
97. R. Wentzcovitch, L. Stixrude, J. J. Rosso, "*Thermodynamic properties and phase relations in mantle minerals investigated by first principles Quasiharmonic theory.* " in *Theoretical and computational methods in mineral physics: Geophysical applications*, R. Wentzcovitch, L. Stixrude, Eds (Berlin, Boston, 2010).
98. W. Wang, Y. Xu, D. Sun, S. Ni, R. Wentzcovitch, Z. Wu, Velocity and density characteristics of subducted oceanic crust and the origin of lower-mantle heterogeneities. *Nat. Commun.* **11**, 64 (2020).
99. R. Caracas, K. Hirose, R. Nomura, M. D. Ballmer, Melt–crystal density crossover in a deep magma ocean. *Earth Planet. Sci. Lett.* **516**, 202-211 (2019).
100. C. B. Agee, Crystal-liquid density inversions in terrestrial and lunar magmas. *Phys. Earth Planet. In.* **107**, 63-74 (1998).
101. J. W. E. Drewitt, M. J. Walter, J. P. Brodholt, J. M. R. Muir, O. T. Lord, Hydrous silicate melts and the deep mantle H_2O cycle. *Earth Planet. Sci. Lett.* **581**, 117408 (2022).
102. N. V. Solomatova, R. Caracas, Buoyancy and Structure of Volatile-Rich Silicate Melts. *J. Geophys. Res. Solid Earth* **126**, e2020JB021045 (2021).
103. N. V. Solomatova, R. Caracas, C. E. Manning, Carbon sequestration during core formation implied by complex carbon polymerization. Nat. Commun. 10, 789 (2019).
104. M. E. Hartley, O. Shorttle, J. Maclennan, Y. Moussallam, M. Edmonds, Olivine-hosted melt inclusions as an archive of redox heterogeneity in magmatic systems. *Earth Planet. Sci. Lett.* **479**, 192-205 (2017).
105. R. L. Helz, E. Cottrell, M. Brounce, K. A. Kelley, Olivine-melt relationships and syneruptive redox variations in the 1959 eruption of Kīlauea Volcano as revealed by XANES. *J. Volcanol. Geotherm. Res.* **333**, 1-14 (2017).
106. M. Brounce, E. Stolper, J. Eiler, Redox variations in Mauna Kea lavas, the oxygen fugacity of the Hawaiian plume, and the role of volcanic gases in Earth's oxygenation. *Proc. Natl. Acad. Sci. U. S. A.* **114**, 8997-9002 (2017).
107. Y. Moussallam, M. Edmonds, B. Scaillet, N. Peters, E. Gennaro, I. Sides, C. Oppenheimer, The impact of degassing on the oxidation state of basaltic magmas: A case study of Kīlauea volcano. *Earth Planet. Sci. Lett.* **450**, 317-325 (2016).
108. M. Gaborieau, M. Laubier, N. Bolfan-Casanova, C. A. McCammon, D. Vantelon, A. I. Chumakov, F. Schiavi, D. R. Neuville, S. Venugopal, Determination of $Fe^{3+}/\Sigma Fe$ of olivine-hosted melt inclusions using Mössbauer and XANES spectroscopy. *Chem. Geol.* **547**, 119646 (2020).
109. D. Mattey, D. Lowry, C. Macpherson, Oxygen isotope composition of mantle peridotite. *Earth Planet. Sci. Lett.* **128**, 231-241 (1994).
110. B. G. Pokrovsky, V. Mavromatis, O. S. Pokrovsky, Co-variation of Mg and C isotopes in late Precambrian carbonates of the Siberian Platform: A new tool for tracing the change in weathering regime? *Chem. Geol.* **290**, 67-74 (2011).
111. A. Geske, J. Zorlu, D. K. Richter, D. Buhl, A. Niedermayr, A. Immenhauser, Impact of

diagenesis and low grade metamorphosis on isotope (δ26Mg, δ13C, δ18O and 87Sr/86Sr) and elemental (Ca, Mg, Mn, Fe and Sr) signatures of Triassic sabkha dolomites. *Chem. Geol.* **332-333**, 45-64 (2012).
112. J. A. Higgins, D. P. Schrag, Constraining magnesium cycling in marine sediments using magnesium isotopes. *Geochim Cosmochim Ac* **74**, 5039-5053 (2010).
113. J. A. Higgins, D. P. Schrag, The Mg isotopic composition of Cenozoic seawater- evidence for a link between Mg-clays, seawater Mg/Ca, and climate. *Earth Planet. Sci. Lett.* **416**, 73-81 (2015).
114. J. A. Higgins, D. P. Schrag, Records of Neogene seawater chemistry and diagenesis in deep-sea carbonate sediments and pore fluids. *Earth Planet. Sci. Lett.* **357**, 386-396 (2012).
115. M. S. Fantle, J. Higgins, The effects of diagenesis and dolomitization on Ca and Mg isotopes in marine platform carbonates: Implications for the geochemical cycles of Ca and Mg. *Geochim Cosmochim Ac* **142**, 458-481 (2014).
116. C. L. Blattler, N. R. Miller, J. A. Higgins, Mg and Ca isotope signatures of authigenic dolomite in siliceous deep-sea sediments. *Earth Planet. Sci. Lett.* **419**, 32-42 (2015).
117. S. Pichat, C. Douchet, F. Albarède, Zinc isotope variations in deep-sea carbonates from the eastern equatorial Pacific over the last 175 ka. *Earth Planet. Sci. Lett.* **210**, 167-178 (2003).
118. S. A. Liu, H. C. Wu, S. Z. Shen, G. Q. Jiang, S. H. Zhang, Y. W. Lv, H. Zhang, S. G. Li, Zinc isotope evidence for intensive magmatism immediately before the end-Permian mass extinction. *Geology* **45**, 343-346 (2017).
119. T. C. Sweere, A. J. Dickson, H. C. Jenkyns, D. Porcelli, M. Elrick, S. H. J. M. van den Boorn, G. M. Henderson, Isotopic evidence for changes in the zinc cycle during Oceanic Anoxic Event 2 (Late Cretaceous). *Geology* **46**, 463-466 (2018).
120. H. Chen, P. S. Savage, F.-Z. Teng, R. T. Helz, F. Moynier, Zinc isotope fractionation during magmatic differentiation and the isotopic composition of the bulk Earth. *Earth Planet. Sci. Lett.* **369-370**, 34-42 (2013).

Acknowledgments

We thank J. Huang, and S.A. Liu for providing some of the intraplate basalt samples. We also thank H. Qin for her kind help in the lab.

Funding: The research was funded by the National Key R&D Program of China (2022YFF0801004), the National Nature Science Foundation of China (Grant 41973010), the National Key R&D Program of China (2019YFA0708404), Fundamental Research Funds for the Central Universities (Grant 2652023001) to S.J. W. W. W acknowledges support from the Fundamental Research Funds for the Central Universities (WK2080000189). S. H acknowledges support from NSF grant EAR-2244895. C. L acknowledges support from the National Natural Science Foundation of China (42025705).

Author contributions: S.J. W conceived and designed the project, and provide fundings. X.H. D, S.J. W, W. W, S. H and S. L contributed to the interpretation of the results, and X.H. D, S.J. W, W. W and S. H wrote and revised the manuscript. Q.L. L and S. W provided olivine oxygen isotopes and trace element analysis. C. L and G. T provided Mössbauer spectra measurement.

Competing interests: The authors declare they have no competing interests.

Data and materials availability: All data are available in the supplementary materials.

Supplementary Materials:

The PDF file includes:

Supplementary Text (Section 1 to 6)

Figures S1 to S11

Legends for Table S1 to S7

Legends for Appendix 1 to 3

References

Other Supplementary Materials for this manuscript includes the following:

Supplementary Tables 1 to 7

Supplementary Appendixes 1 to 3

FIGURE CAPTURES

Fig. 1. Geological and geochemical background of Cenozoic intraplate basalts from eastern China. (A) Simplified geological map of eastern China and the distribution of Cenozoic intraplate basalts. **(B)** Stagnant Pacific slab beneath eastern China revealed by seismic tomography along the A-A' profile, modified from Huang and Zhao (*9*). **(C)** Primitive mantle (PM) (*69*) normalized incompatible element diagram for EC Cenozoic basalts (yellow patterns), compared with OIB with HIMU (high μ, $\mu = {}^{238}U/{}^{204}Pb$) affinity, continental crust and carbonatite. Bermuda HIMU lavas are from Mazza et al. (*49*). The averages of other HIMU (St Helena and Cook Austral) lavas are compiled from GEOROC dataset (see data source in Supplementary Appendix 1). The average of continental crust is from Rudnick and Gao (*70*). The deep diamond inclusion (11-ON-ZIZ) with HIMU-like incompatible trace elemental signatures is from Huang et al. (*5*). The averages of Group-1 kimberlite and high-Mg carbonatite are from Weiss et al. (*71*). The averages of calcio and magnesio carbonatites are from Hoernle et al. (*72*).

Fig. 2. Wet-chemistry $Fe^{3+}/\sum Fe$ values versus Mössbauer spectra $Fe^{3+}/\sum Fe$ values (A), olivine $\delta^{18}O$ (B), olivine V/Sc (C), and MgO (D) for EC Cenozoic intraplate basalts. $Fe^{3+}/\sum Fe$ values measured using wet-chemistry and Mössbauer spectrometry are reported in Supplementary Tables 1 and 3, respectively. The triangle represents the USGS basalt standard BCR-2. Error bars in (A) reflect ± 10% error for wet chemistry $Fe^{3+}/\sum Fe$ values and 1 s. d. for Mössbauer spectra $Fe^{3+}/\sum Fe$ values. Olivine $\delta^{18}O$ and V/Sc data are reported in Supplementary Table 4. Data points represent the average of analyzed olivine grains from individual EC basalts. A histogram plot of all analyzed olivine $\delta^{18}O$ (n = 198) and a plot of $\delta^{18}O$ versus V/Sc for all analyzed olivine grains are shown in Supplementary Fig. 4. Error bars in (B) and (C) represent 2 s. e. for olivine $\delta^{18}O$ and V/Sc of individual samples. Samples with LOI > 3 wt% are shown in red dashed.

Fig. 3. Corrected $Fe^{3+}/\sum Fe$ values versus U/Pb (A) and Th/Ba (B) for EC Cenozoic intraplate basalts. Data of EC Cenozoic intraplate basalts are shown in red circles and reported in Supplementary Table 1, with those with LOI > 3 wt% shown in red dashed. $Fe^{3+}/\sum Fe$ values are corrected for olivine crystal fractionation or accumulation. Error bars represent ± 10% for $Fe^{3+}/\sum Fe$ values of EC Cenozoic intraplate basalts. Data of arc basalts are shown in yellow square and provided in Supplementary Appendix 2. The "most parental" $Fe^{3+}/\sum Fe$ values of OIB from each hotspot location are compiled from Brounce et al. (*19*) and Moussallam et al. (*2*). A complete data source including $Fe^{3+}/\sum Fe$ and average elemental compositions of OIB is provided in Supplementary Appendix 3. Error bars represent 2 s.e. for OIB averages. The average $Fe^{3+}/\sum Fe$ values of MORB and primitive mantle (PM) are from Zhang et al. (*18*) and Canil et al. (*28*), respectively. The trace element compositions of average MORB and PM are from McDonough and Sun (*69*). HOME: Highly Oxidized Mantle Endmember.

Fig. 4. Corrected $Fe^{3+}/\sum Fe$ values versus CaO/Al_2O_3 (A), Hf/Hf* (B), Ti/Ti* (C), Zr/Nd (D), $\delta^{26}Mg$ (E), and $\delta^{66}Zn$ (F) for EC Cenozoic intraplate basalts. $Fe^{3+}/\sum Fe$ values are corrected for olivine crystal fractionation or accumulation. Legend and data source are same as Figure 3. The orange diamond represents multiphase diamond inclusion (11-ON-ZIZ) from Huang et al. (*5*). $Hf/Hf^* = Hf_N/(Sm_N \times Nd_N)^{0.5}$; $Ti/Ti^* = Ti_N/(Nd_N^{-0.055} \times Sm_N^{0.333} \times Gd_N^{0.722})$; $\delta^{26}Mg = ({}^{26}Mg/{}^{24}Mg)_{sample}/({}^{26}Mg/{}^{24}Mg)_{DSM3}-1) \times 1000$; $\delta^{66}Zn = ({}^{66}Zn/{}^{64}Zn)_{sample}/({}^{66}Zn/{}^{64}Zn)_{JMC\ 3\text{-}0749L}-1) \times 1000$.

Fig. 5. Olivine $\delta^{18}O$ values versus U/Pb (A), Th/Ba (B), Hf/Hf* (C), and Ti/Ti* (D) for EC Cenozoic intraplate basalts. Data of EC Cenozoic intraplate basalts are reported in Supplementary Tables 1 and 4 and shown in red circle. Olivine $\delta^{18}O$ values of EC basalts from the literature (*47*) are shown in grey square. The $\delta^{18}O$ values of MORB and primitive mantle (PM) are from Valley et al. (*73*) and Mattey et al. (*21*), respectively. The trace element compositions of average MORB and PM are from McDonough and Sun (*69*). The $\delta^{18}O$ values and trace element compositions of PIC (Phlogopite-Ilmenite-Clinopyroxene) are from Wang et al. (*46*) and Fitzpayne et al. (*74*), respectively.

Fig. 6. Formation mechanism of HOME. (A) Density-pressure profiles of melts and diamond. Solid yellow: diamond; dashed orange: dry MORB ($Mg_6Ca_6Fe_5Si_{27}Al_{10}Na_3O_{88}$): dashed green: MORB with 4.9 wt% H_2O ($Mg_6Ca_6Fe_5Si_{27}Al_{10}Na_3H_{18}O_{97}$); dashed blue ($Mg_6Ca_6Fe_5Si_{27}Al_{10}Na_3C_4O_{96}$): MORB with 5.3 wt% CO_2. Data are reported in Supplementary Table 6. The density-pressure profiles of a variety of carbonate melts are from Massuyeau et al. (*75*). **(B)** The melting curves of carbonated MORB and carbonated peridotites compared to subduction geotherms and ambient mantle adiabat, modified from Thomson et al. (*42*) and Dasgupta (*76*). **(C)** Cartoon showing the formation of HOME in the BMW. Low-degree melting of stagnant carbonated Pacific slab generates carbonated melts. With excess C^{4+} replenished from subducted slabs, carbon-iron redox reaction happened in the melts ($4Fe^{2+} + C^{4+} \rightarrow 4Fe^{3+} + C^0$), and efficient separation of the newly-formed diamond from the melts due to density difference would have elevated the melts' $Fe^{3+}/\sum Fe$, forming the HOME. These melts have HIMU elemental signatures, which subsequently metasomatizes the ambient peridotites. The interaction would have promoted carbon-iron redox reaction to precipitate diamond from melts and meanwhile to elevate the $Fe^{3+}/\sum Fe$ of carbonated peridotites. Excess CO_2 from the subducted slab derived carbonated melts decreases the solidus of metasomatized peridotites, leading to partial melting of the high-$Fe^{3+}/\sum Fe$ carbonate-metasomatized peridotitic domains to produce melts inherited the HOME signature.

852 **Fig. 1**

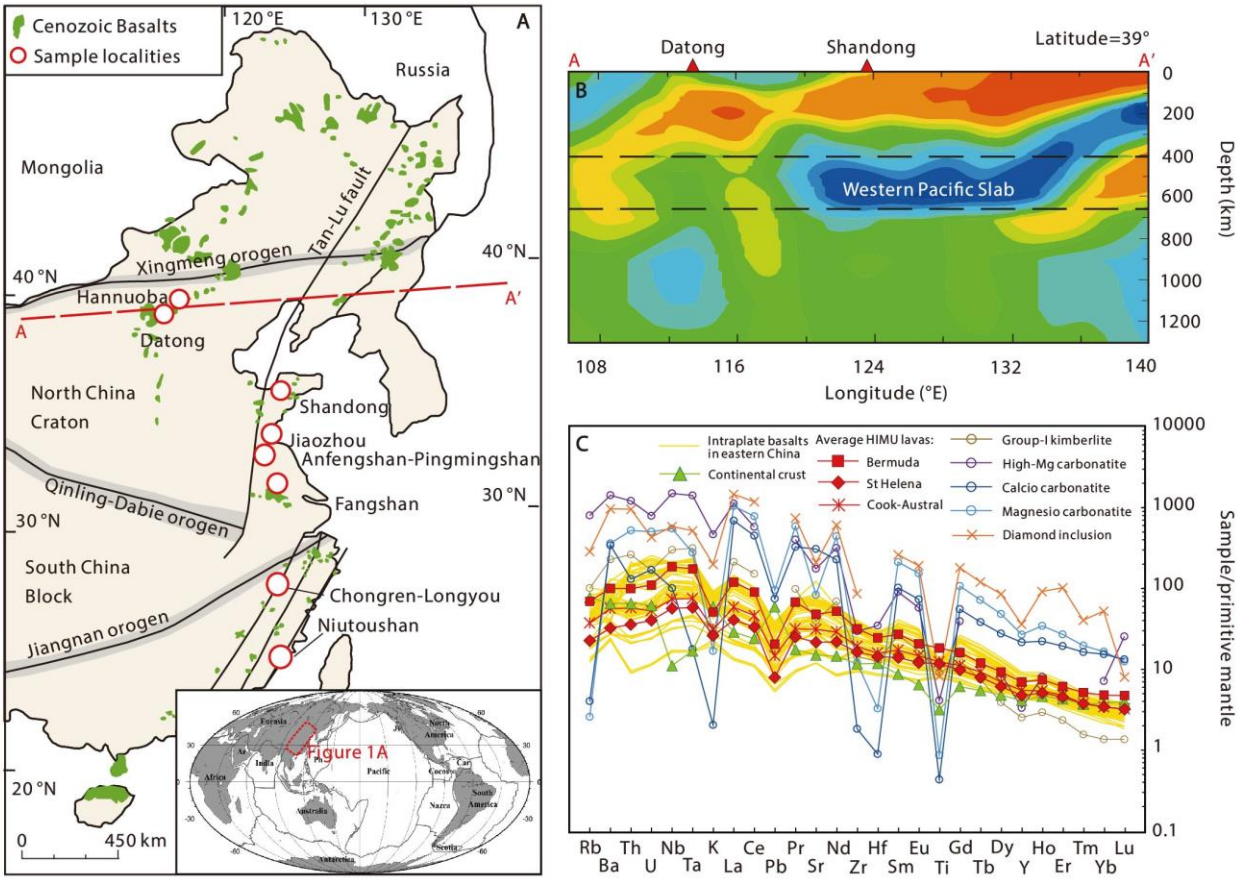
Cenozoic Basalts
Sample localities
120 °E
130 °E
A
Russia
Mongolia
Tan-Lu fault
Xingmeng orogen
40 °N
40 °N
Hannuoba
A'
A
Datong
North China
Craton
Shandong
Jiaozhou
Anfengshan-Pingmingshan
Qinling-Dabie orogen
Fangshan
30 °N
30 °N
South China
Block
Chongren-Longyou
Niutoushan
Jiangnan orogen
Figure 1A
20 °N
0
450 km
B
Datong
Shandong
Latitude=39°
A
A'
Western Pacific Slab
0
200
400
600
800
1000
1200
Depth (km)
108
116
124
132
140
Longitude (°E)
C
Intraplate basalts in eastern China
Continental crust
Average HIMU lavas:
Bermuda
St Helena
Cook-Austral
Group-I kimberlite
High-Mg carbonatite
Calcio carbonatite
Magnesio carbonatite
Diamond inclusion
10000
1000
100
10
1
0.1
Sample/primitive mantle
Rb Th Nb K Ce Pr Nd Hf Eu Gd Dy Ho Tm Lu
Ba U Ta La Pb Sr Zr Sm Ti Tb Y Er Yb

853

Fig. 2

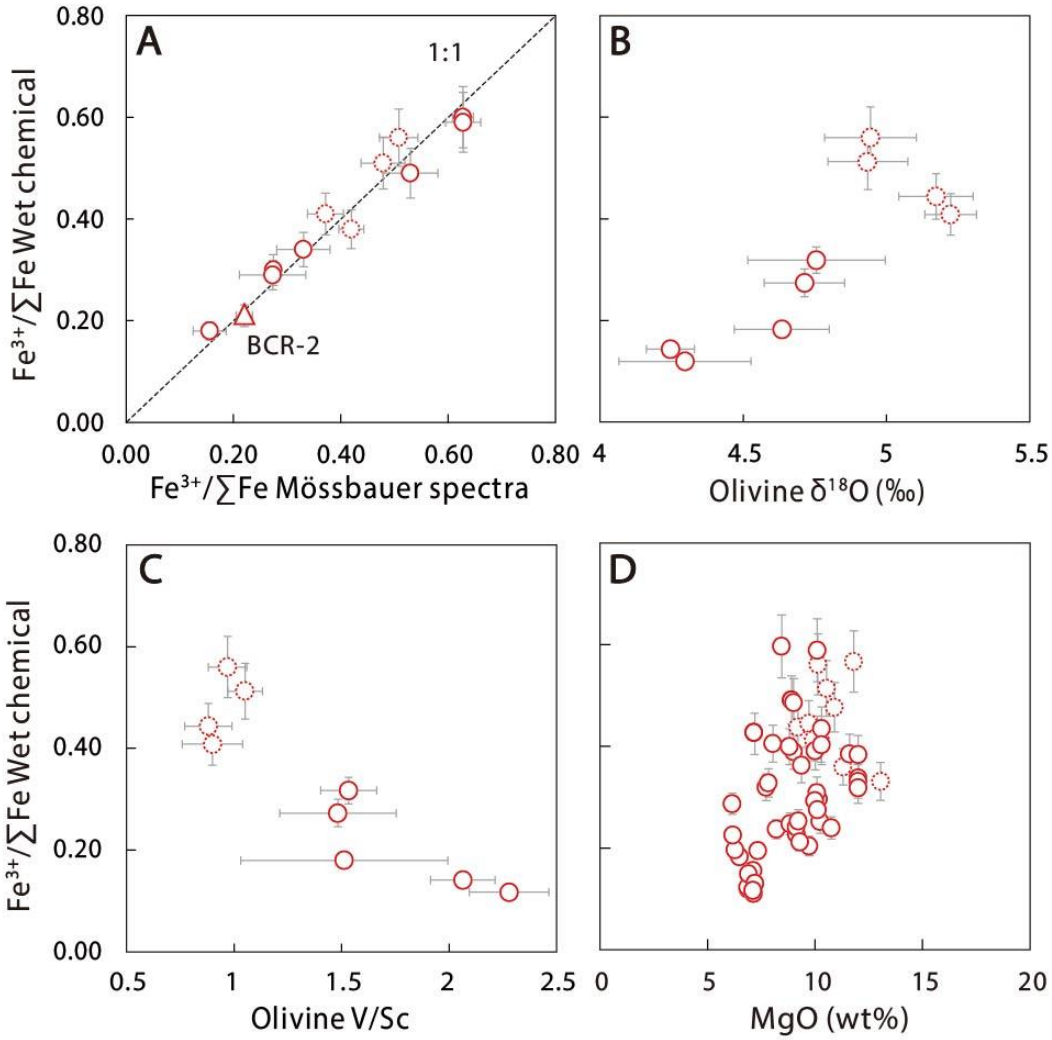
A
1:1
BCR-2
Fe³⁺/∑Fe Wet chemical
Fe³⁺/∑Fe Mössbauer spectra
0.00
0.20
0.40
0.60
0.80
B
Olivine δ¹⁸O (‰)
4
4.5
5
5.5
C
Olivine V/Sc
0.5
1
1.5
2
2.5
D
MgO (wt%)
0
5
10
15
20

Fig. 3

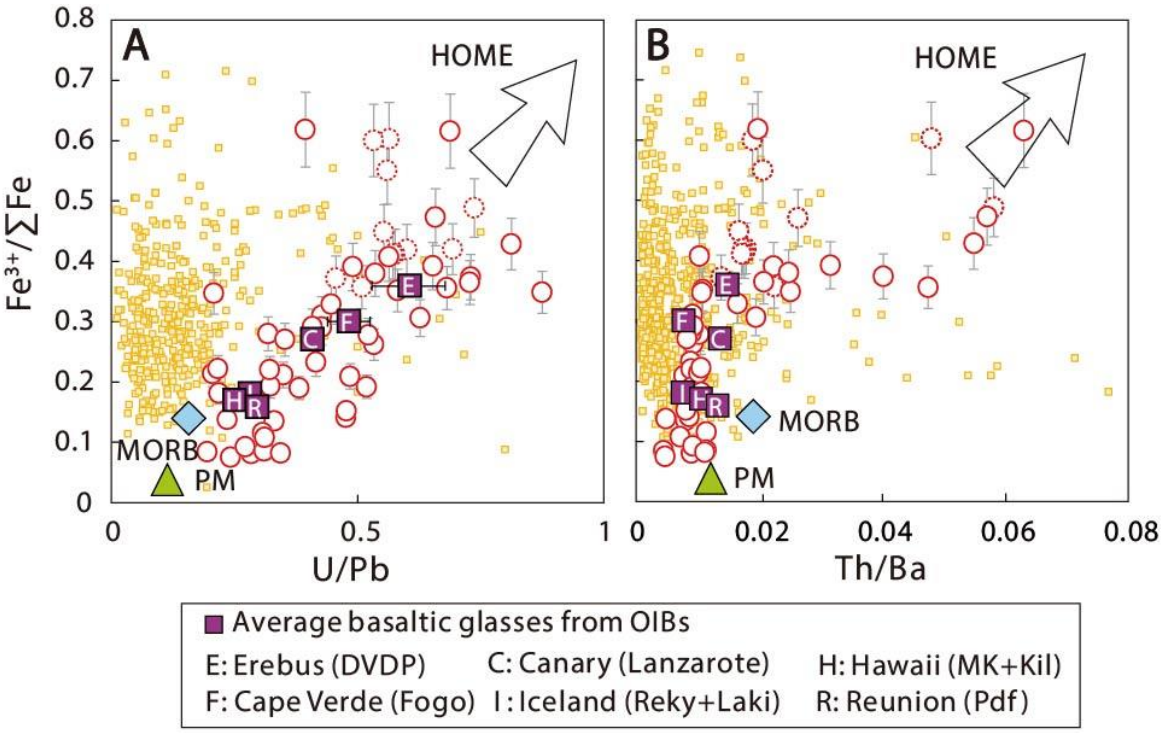
A
B
HOME
HOME
$Fe^{3+}/\sum Fe$
U/Pb
Th/Ba
MORB
PM
MORB
PM
E
F
C
H
R
I
0.8
0.7
0.6
0.5
0.4
0.3
0.2
0.1
0
0
0.5
1
0
0.02
0.04
0.06
0.08
Average basaltic glasses from OIBs
E: Erebus (DVDP)
C: Canary (Lanzarote)
H: Hawaii (MK+Kil)
F: Cape Verde (Fogo)
I : Iceland (Reky+Laki)
R: Reunion (Pdf)

Fig. 4

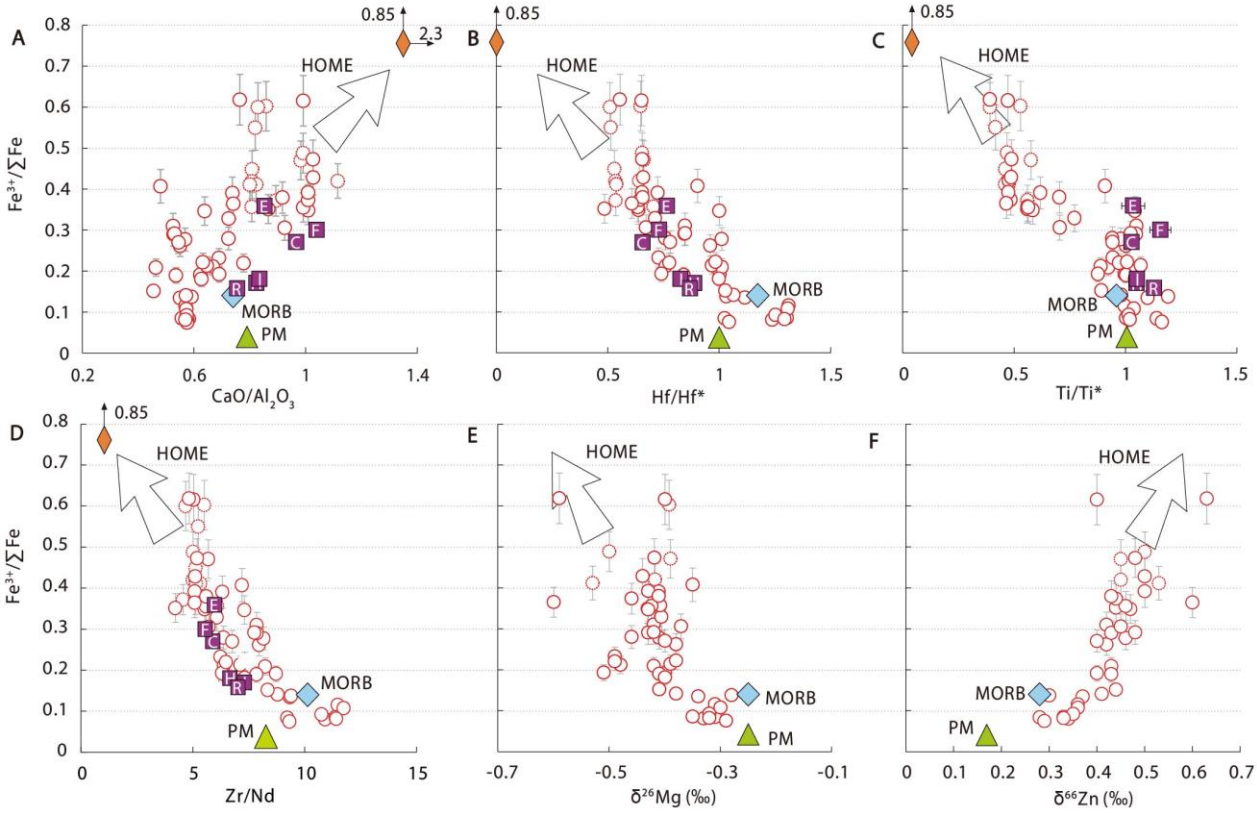
A
B
C
D
E
F
HOME
MORB
PM
0.85
2.3
Fe³⁺/∑Fe
CaO/Al₂O₃
Hf/Hf*
Ti/Ti*
Zr/Nd
δ²⁶Mg (‰)
δ⁶⁶Zn (‰)

860 **Fig. 5**

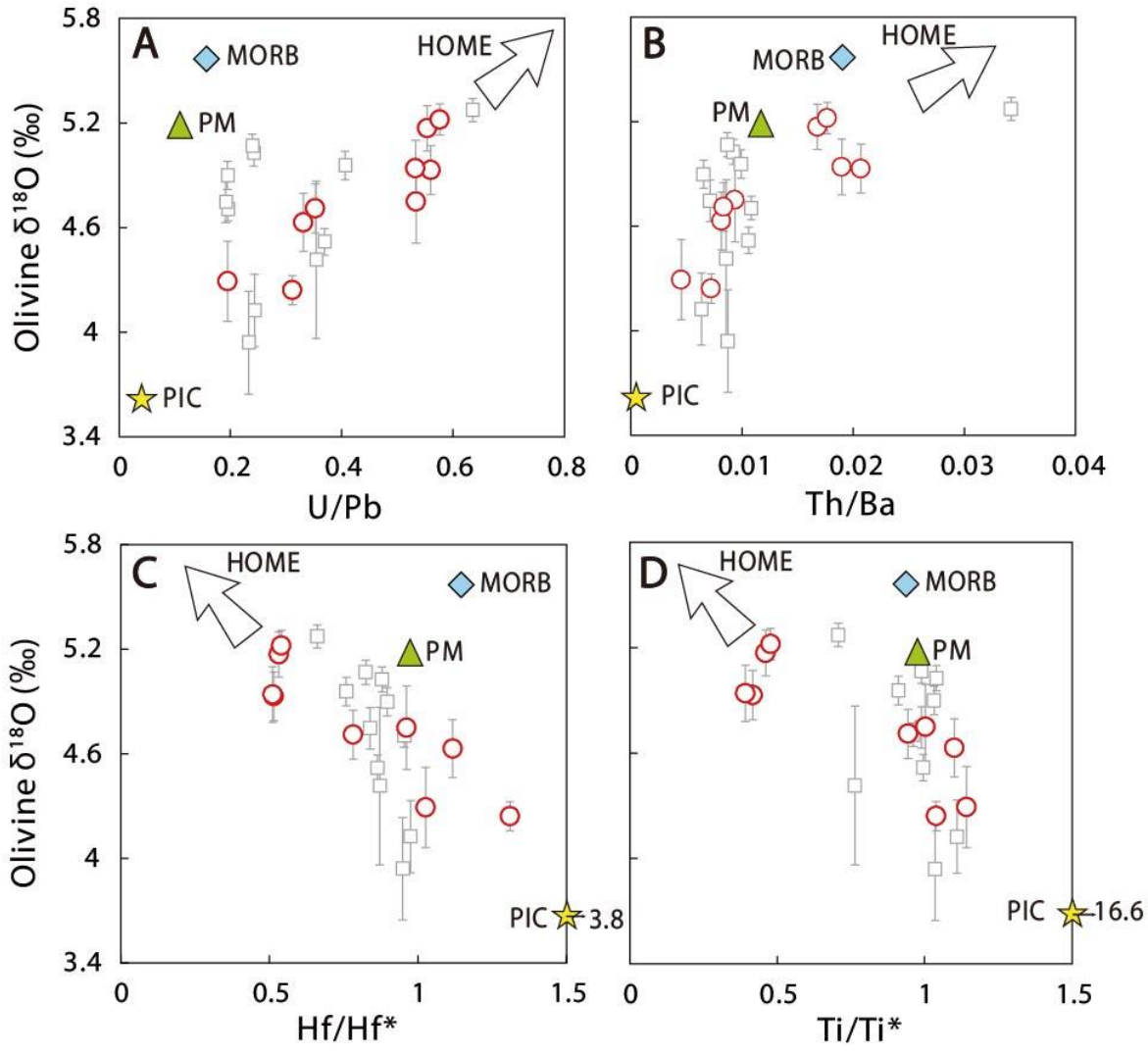
A
MORB
HOME
PM
PIC
Olivine δ18O (‰)
5.8
5.2
4.6
4
3.4
0
0.2
0.4
0.6
0.8
U/Pb
B
MORB
HOME
PM
PIC
0
0.01
0.02
0.03
0.04
Th/Ba
C
HOME
MORB
PM
PIC 3.8
0
0.5
1
1.5
Hf/Hf*
D
HOME
MORB
PM
PIC 16.6
0
0.5
1
1.5
Ti/Ti*

861

Fig. 6

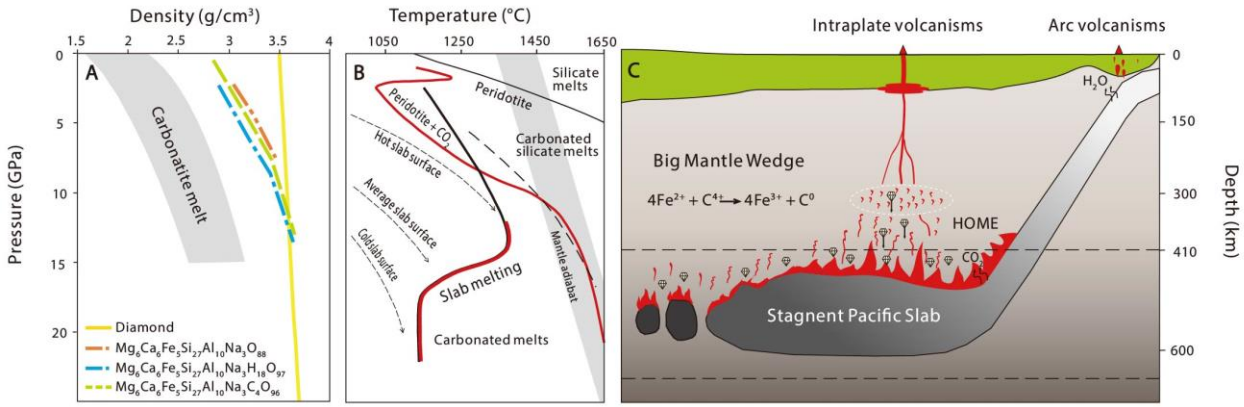
Density (g/cm³)
1.5
2
2.5
3
3.5
4
Pressure (GPa)
0
5
10
15
20
A
Carbonatite melt
Diamond
Mg6Ca6Fe5Si27Al10Na3O88
Mg6Ca6Fe5Si27Al10Na3H18O97
Mg6Ca6Fe5Si27Al10Na3C6O96
Temperature (°C)
1050
1250
1450
1650
B
Silicate melts
Peridotite
Peridotite + CO2
Carbonated silicate melts
Hot slab surface
Average slab surface
Cold slab surface
Slab melting
Mantle adiabat
Carbonated melts
Intraplate volcanisms
Arc volcanisms
C
H2O
Big Mantle Wedge
4Fe2+ + C4+ → 4Fe3+ + C0
HOME
CO2
Stagnent Pacific Slab
0
150
300
410
600
Depth (km)

Science Advances
AAAS

Supplementary Materials for

Highly oxidized intraplate basalts and deep carbon storage

Dong *et al.*

*Corresponding author. Email: wsj@cugb.edu.cn (S.-J. Wang); wwz@ustc.edu.cn (W.-Z. Wang)

This PDF file includes:

Supplementary Text
Figs. S1 to S11
Legends for Table S1 to S7
Legends for Appendix 1 to 3
References

Other Supplementary Materials for this manuscript include the following:

Supplementary Table 1 to 7
Appendix S1 to S3

Supplementary Text

Supplementary Section 1

Geological Setting and samples

Cenozoic intraplate basalts in eastern China are widely distributed along the coastal provinces and adjacent offshore shelf extending over 4000 km. Representative Cenozoic intraplate basalts from eight localities in eastern China were analyzed for $Fe^{3+}/\sum Fe$ value in this study. In a total alkali vs silica (TAS) diagram, studied samples ranges from nephelinite to basaltic andesite (Fig. S1). Their FeO_{total} range from 9.7 to 14.5 wt% (*77-82*).

Datong volcanic field (DVF) is located in the northern part of the Trans-North China Orogen. The DVF erupted at 0.74 Ma and 0.4 Ma (*83, 84*). Eighteen fresh samples analyzed herein are porphyritic olivine basalts, where phenocrysts are olivine, plagioclase and clinopyroxene, and the groundmass is composed of plagioclase, clinopyroxene and needle-shaped Fe–Ti oxide (*77*). These samples range from tholeiitic basalt, alkaline trachybasalt to basanite (*77*), with their major, trace element and Mg-Zn isotopic compositions reported in Wang and Liu (*77*).

Hannuoba basaltic plateau is located along the northern margin of the Trans-North China Belt. Hannuoba basalts have K-Ar ages of 14-22 Ma (*78*). Five samples from Hannuoba analyzed in this study are porphyritic alkaline basalts (*78*). They have rare and small fresh olivine phenocrysts with a groundmass of plagioclase, clinopyroxene, olivine, and opaque minerals (*78*). Their major and trace elements have been studied by Qian et al. (*78*), and Mg isotopic compositions were reported in Li et al. (*16*).

Shandong basaltic field is located in the North China carton. The Cenozoic alkaline magmatism in Shandong took place during two periods: 24.0-10.3 Ma and 8.7-0.3 Ma (15, *85*). The early magmatism was voluminous and characterized by large volcanoes densely distributed in a narrow area near the Tan-Lu Fault. Most samples are fresh except a few samples from Fangshan and Mashan, whose olivine phenocrysts are partially altered to iddingsite (*79*). All samples have minor olivine as phenocrysts in a groundmass of olivine, Ti-magnetite, nepheline, and glass (*79*). These samples are classified as basanite and nephelinite (*79*). Their $Fe^{3+}/\sum Fe$ have been analyzed by Sheng et al. (*86*), and our duplicated analyses of $Fe^{3+}/\sum Fe$ for a selective set of samples agree well within 3% with those reported in Sheng et al. (*86*) (Table S1). Comparison of $Fe^{3+}/\sum Fe$ values between unaltered and slightly altered samples suggests that iddingsitization does not have an impact on the bulk-rock $Fe^{3+}/\sum Fe$ (*86*). Their major and trace element compositions were reported by Zeng et al. (*15*) and Zeng et al. (*79*), and their Mg-Zn isotope were reported in Zeng et al. (*79*) and Wang et al. (*87*).

Pingmingshan – Anfengshan is located in the Sulu orogenic belt. Pingmingshan and Anfengshan basalts have K-Ar ages of 7.3-12.3 and 4.0-6.4 Ma, respectively (*85*). Five samples from Pingmingshan and three samples from Anfengshan were analyzed in this study. Most of the studied samples are fresh, except for 13AFS9 and 13AFS10, whose olivine phenocrysts were partially altered to iddingsite. These samples are porphyritic basanite (*80*), where phenocrysts consist predominantly of olivine in the Anfengshan basalts and olivine, clinopyroxene, and plagioclase in the Pingmingshan basalts (*80*).

Their groundmass mainly consists of plagioclase, olivine, augite, nepheline, magnetite and glass. Their major and trace element compositions have been studied by Huang et al. (*80*). Their Mg-Zn isotopic compositions were reported in Li et al. (*16*) and Liu et al. (*39*).

Jiaozhou is located in Jiaolai basin in the North China carton. Jiaozhou basalts have K-Ar ages of 71.9 Ma (*81*). Four samples studied in this study are porphyritic basanites (*81*), where phenocrysts consist of fresh pyroxene and olivine and groundmass mainly consists of plagioclase, olivine, pyroxene and Fe-Ti oxide (*81*). Their major, trace element and Sr-Nd isotopic compositions have been studied by Meng et al. (*81*). The Mg isotope compositions of four samples were reported in Li et al. (*16*).

Fangshan is located in the northeast of the South China Block. Fangshan basalts were dated at 2.9-3.5 Ma by K-Ar method (*80*). Five fresh samples analyzed in this study are porphyritic trachybasalt (*80*), where phenocrysts consist of olivine and clinopyroxene and the groundmass mainly consists of plagioclase, olivine, augite, nepheline, magnetite and glass. Their major, trace element and Mg-Zn isotope compositions were reported in Huang et al. (*80*) and Liu et al. (*39*).

Longyou is located in the east of the South China Block. Longyou basalts were dated at 9.4-9.0 Ma by K-Ar method (*80*). They are porphyritic basanites, and phenocrysts consist of olivine and clinopyroxene. Their groundmass mainly consists of plagioclase, olivine, augite, nepheline, magnetite and glass. Two samples from Longyou are analyzed in this study. Sample 10LYSK13 is fresh, whereas 10LYSK11 is slightly altered with olivine phenocrysts partially replaced by iddingsite. These two samples show very similar $Fe^{3+}/\sum Fe$ values of 0.33 and 0.34, respectively, supporting that iddingsitization does not change the bulk-rock $Fe^{3+}/\sum Fe$ (Table S1). Their major, trace element and Mg-Zn isotope compositions were reported in Li et al. (*16*) and Liu et al. (*39*).

Niutoushan is located in the southeast of the South China Block. Niutoushan basalts were dated at 19.2-11.7 Ma by K-Ar method (*82*). An alkaline basalt sample from Niutoushan was analyzed in this study. This sample has fresh olivine and pyroxene as phenocrysts in a groundmass of plagioclase and pyroxene (*82*). Its major and trace element compositions were reported by Yang (*82*) and Mg isotopic compositions were reported in Li et al. (*16*).

Supplementary Section 2

$Fe^{3+}/\sum Fe$ correction for crystal fractionation

Different degree of crystal fractionation prior to eruption may cause the $Fe^{3+}/\sum Fe$ variation, although this effect is thought to be minimal (*88*). Here, we corrected $Fe^{3+}/\sum Fe$ data to the primary magma composition, following the method of Sossi et al. (*89*). Since all of our studied basalts have MgO > 6 wt%, it is assumed that olivine is the only crystal phase removed from or added to the melts (*89*). Olivine in equilibrium with melt is calculated using $K_{D}^{Fe-Mg}_{Ol-Melt}$ = 0.3 (defined as the molar Fe^{2+}/Mg of the liquid divided by Fe/Mg of coexisting olivine (*90*)), and it is added or subtracted at a step of 1 wt% until $Mg\#_{melt}$ = 0.72, equilibrium with mantle olivine at Fo_{90}. Considering that olivine in an

oxidized mantle may have a lower Fo content than the normal mantle (*91*), we did another set of correction to equilibrate the melt with mantle olivine at Fo_{85}. The MgO and FeO composition of the olivine crystallizing is given by:

$$\left(\frac{Fe}{Mg}\right)_{Ol} = K_{D\,Ol-Melt}^{Fe-Mg}\left(\frac{Fe}{Mg}\right)_{Melt}$$

where Fe = FeO (wt%)/71.845 and Mg= MgO (wt%)/40.3. The composition of the olivine is iterated every 1%, and the composition of the melt + olivine mixture is given by mass balance:

$$M_{Melt}^{F_n} = \left(1-(F_n - F_{n-1})\right)M_{Melt}^{F_{n-1}} + (F_n - F_{n-1})M_{Ol}^{F_n}$$

M refers to the concentration of an element, and F is the fraction of olivine, which ranges from $F_1, F_2 \ldots F_n$, where n is the number of iterations. The modelling results show that olivine fractional crystallization or accumulation may have shifted $Fe^{3+}/\sum Fe$ data by no more than 0.08, and the corrected $Fe^{3+}/\sum Fe$ for melts equilibrated with Fo_{90} or Fo_{85} olivines agree with each other within 24% (Fig. S7).

Supplementary Section 3

Partial melting models

A non-modal incremental batch melting model is used to evaluate the re-distribution of Fe^{2+} and Fe^{3+} during partial melting (*92*). Initial modal abundances of olivine, clinopyroxene, orthopyroxene, and garnet are assumed to be 0.53, 0.27, 0.18, and 0.02, respectively (*93*). Melting reactions of partial melting of garnet peridotite were taken from Walter et al. (*93*). Garnet and clinopyroxene in peridotite were modeled to be exhausted at 10% and 23% degree of melting. Partition coefficients for Fe^{2+} ($D_{Fe^{2+}}$) and Fe^{3+} ($D_{Fe^{3+}}$) of mantle minerals are from Wang et al. (*94*). The mass melted at each step was set to 1% (F_0) of the bulk mass. Then the melting degree relative to the evolving residue of each step i (f_i) can be calculated according to

$$f_i = \frac{F_0}{1-(i-1)F_0}$$

At each melting increment, the modal abundance of each phase and its Fe^{2+} and Fe^{3+} concentration is calculated by mass balance from the original source mineralogy and Fe^{2+} and Fe^{3+} contents of mineral coupled with their partition coefficients (*94*). Melting reactions are defined using liquid modes (P values):

$$n_{min}^{r} = n_{min}^{0} - (F \times P_{min})$$

Where n_{min}^{r} and n_{min}^{0} represent model abundance of residual minerals and initial minerals, respectively. F indicates degree of partial melting. P_{min} describes the relative proportion of a given mineral in the melting reaction. The Fe^{2+} and Fe^{3+} content of the bulk residue is then calculated as the weighted sum of the residual mineral modal abundances (normalized to 100%) and their contents. The partition coefficients at each melting increment of melt and residue (D_{l-r}) are calculated using the Fe^{2+} and Fe^{3+} content of the minerals (C_{min}) and partition coefficients of melt and minerals (D_{l-min}):

$$D_{l-r} = \sum_{i=1}^{n} [n_i * C_{min}] \times \sum_{i=1}^{n} [n_i * D_{l-min}]$$

Where n represents normalized model abundance of minerals. The element abundance in the instant melt of step i C_i^l can be calculated by using the equation of

$$C_i^l = \frac{C_{i-1}^r}{D_{l-r} + (1 - D_{l-r})f_i}$$

We also used a fractional melting model to determine the Fe^{2+} and Fe^{3+} content in the melts for comparison:

$$C_i^l = C_{i-1}^r \times \frac{1}{D_{l-r}} (1 - f_i)^{(\frac{1}{D_{l-r}} - 1)}$$

where the element abundance in the residue of step n $C_n^r = D * C_n^l$, and the element content of aggregate melt of step i C_i^{melt} are

$$C_i^{melt} = \sum_{i=0}^{n} C_i^l / i$$

Our modelling shows that the $Fe^{3+}/\sum Fe$ value of melts does not differ significantly between batch melting and fractional melting (Fig. S8). Partial melting of a peridotitic mantle source with a normal-mantle $Fe^{3+}/\sum Fe$ of 0.036 (*28*) cannot produce the high-$Fe^{3+}/\sum Fe$ value observed in EC basalts (Fig. S8). In order to produce the high $Fe^{3+}/\sum Fe$ as high as 0.6 in EC basalts, the $Fe^{3+}/\sum Fe$ of the mantle source must be elevated to, for example, ~0.30 if 3% partial melting degree is assumed (Fig. S8).

Supplementary Section 4

Mixing model calculation

We calculate the amount of subducted carbonate required to produce the observed high-$\delta^{66}Zn$ and low-$\delta^{26}Mg$ endmember for the HOME using a mixing model of subducted oceanic crust and carbonate. Experimental studies have shown that with increasing pressure during subduction, the stable carbonate mineral changes from calcite, to calcite/dolomite, and to dolomite/magnesite (e.g. *95*). Therefore, dolomite/magnesite was taken as an endmember in the mass balance calculations. The subducted oceanic crust is assumed to be a mixture of carbonate minerals and MORB. The modelling results are plotted in Fig. S10.

Our modelling suggests that involving small amounts of dolomite and magnesite in the melting reactions would lead to a significant deviation of the Mg-Zn isotopic compositions of the melt from the normal mantle range, and different carbonate species have different effects on the Mg-Zn isotopic compositions of resulting melts due to the distinct elemental contents and initial isotopic compositions of dolomite and magnesite. Overall, in order to produce the observed high-$\delta^{66}Zn$ and low-$\delta^{26}Mg$ HOME, 10-20% of

carbonates are needed in the melting reaction during the partial melting of carbonated oceanic crust (Fig. S10A).

The Mg-Zn isotopic variations observed in the EC basalts can be explained by a mixture of the HOME (15% carbonate + 85% MORB) and asthenospheric peridotite (Fig. S10B). Modelling parameters are provided in Supplementary Table 7.

Supplementary Section 5

Computational details of the melt-diamond density crossover at mantle depth

We performed first-principles molecular dynamics (FPMD) simulations based on density functional theory (DFT) using the Vienna *ab initio* simulation package (VASP). The local density approximation (LDA) and projector augmented wave method were adopted for the exchange-correlation functional. The energy cutoff was 600 eV. The gamma point was used for Brillouin zone summations over the electronic states. Previous studies found that LDA works better than the generalized gradient approximation (GGA) in predicting many properties of silicates including equation of state and elasticity (*96-98*). Single-particle orbitals were populated based on the Fermi–Dirac statistics. All spin-polarized FPMD simulations were performed in the NVT (constant number of atoms N, volume V, and temperature T) thermodynamic ensemble with a fixed temperature controlled by a Nosé thermostat. The time step was set to 1 fs. We focus on three types of silicate melts with mid-ocean ridge basalt (MORB) compositions, $Mg_6Ca_6Fe_5Si_{27}Al_{10}Na_3O_{88}$ (dry MORB), $Mg_6Ca_6Fe_5Si_{27}Al_{10}Na_3H_{18}O_{97}$ (MORB with 4.9 wt.% water), and $Mg_6Ca_6Fe_5Si_{27}Al_{10}Na_3C_4O_{96}$ (MORB with 5.3 wt.% CO_2) to model the water- and carbon-bearing basaltic melts (Table S5). We did not introduce a Hubbard U correction for Fe atoms, as Caracas et al. (*99*) found that a +U correction does not significantly improve the calculated properties. The initial melt configurations at different volumes were prepared by melting the structures at 6000 K and down to 3000 K for 10 ps, and then, we ran NVT simulations at 1700 K for at least 40 ps. Pressures at different volumes were derived by averaging the pressure for each time step after the equilibration. The calculated results together with the chemical compositions were listed in Table S6.

Our calculated results show that at 1700 K, the density of dry basaltic melt increases from 3.046 g/cm^3 at 2.2 GPa to 3.461 g/cm^3 at 7.5 GPa. A linear interpolation suggests a density of ~ 3.35 g/cm^3 at 6 GPa, which is higher than the measured values (3.23 g/cm^3) at 5.9 GPa and 1673 K using the sink-float method (*100*). This is typical for the LDA, which underestimates the volumes of silicate minerals and hence overestimates their densities (*97*). A pressure correction of ~ +1.5 GPa is required to bring the LDA results into agreement with the experimental data. In contrast, the GGA underestimates the density of silicate minerals, and it was suggested that the pressure correction should be at least -2.5 GPa to match the literature data (*101*).

The density of MORB melt with 4.9 wt.% water ranges from 2.902 g/cm^3 at 2.2 GPa to 3.638 g/cm^3 at 13.5 GPa, 1700 K. Compared with dry MORB melt, the density of this hydrous MORB melt is lowered by ~ 0.18 g/cm^3, corresponding to a decrease of 0.037 g/cm^3 per 1 wt.% H_2O. Recently, Drewitt et al. (*101*) conducted FPMD simulations on

MgO-SiO_2-H_2O melts using GGA and found that the incorporation of 1.0 wt.% water can reduce the density of $MgSiO_3$ melt by ~0.043 g/cm^3, which is similar to our results.

The density of MORB melt with 5.3 wt.% CO_2 is lower than that of dry MORB melt but higher than that of MORB melt with 4.9 wt.% H_2O (Table S6). The incorporation of CO_2 into MORB melt also decreases its density, the CO_2 effect on is weaker than the H_2O effect. In comparison, the density of MORB melt only decreases by ~0.015 g/cm^3 per 1 wt.% CO_2. Such a magnitude is similar to the CO_2 effect on the density of pyrolite melt at 3000 K calculated by FPMD simulations using GGA (*102, 103*).

Our simulations together with previous studies on diamond show that diamond is always denser than MORB deeper than the bottom of upper mantle (~12-14 GPa). As the density of silicate melt increases with Fe content but decreases with H_2O and CO_2 contents, the intersection of the density lines of diamond and silicate melt could be changed by 1-2 GPa. This variation caused by the chemical composition does not change the conclusion that diamonds formed in deep-sourced carbon-bearing silicate melts via the redox reaction will descend to the bottom of melt and the residual melt, if it is separated from diamonds, would be enriched in Fe^{3+}.

Supplementary Section 6

The amount of carbon storage

In order to estimate the area of Cenozoic basalt exposed on the land of eastern China, Chen et al. (*51*) utilized a digital-image processing program to extract the distribution information of Cenozoic basalts by pixel from the geological map, and overlaid on the high-precision geomorphologic map. The specific methods are as follows.

The geological and geomorphic map of eastern China attached in GeoMapApp are drawn by Mercator projection. The ratio of basalt eruption area S1 to the Earth surface area S of the region is equal to the ratio of basalt image area P1 in the Mercator projection graph to the image area P of the region, within the latitude of 1 °, between a certain longitude.

$$\frac{S_1}{S} = \frac{P_1}{P}$$

The image area in the Mercator projection graph can be calculated by photoshop software. The Earth surface area S between latitude λ_1 to latitude λ_2 ($\lambda_2 = \lambda_1 + 1$) and longitude ϕ_1 to longitude ϕ_2 ($\phi_2 > \phi_1$) can be obtained by spherical calculation formula:

$$S = 2\pi R^2(\sin\lambda_2 - \sin\lambda_1) \times \frac{(\phi_2 - \phi_1)}{360}$$

Therefore, the basalt eruption area S_1 can be calculated as

$$S_1 = \frac{P_1}{P} 2\pi R^2(\sin\lambda_2 - \sin\lambda_1) \times \frac{(\phi_2 - \phi_1)}{360}$$

where *R* represents Earth's radius, with an average value of 6371 km. The total area of basalt in a certain area (S_{total}) is the sum of the areas in each latitude.

$$S_{total} = S_1 + S_2 + S_3 + \cdots S_n$$

The results show that the total area of Cenozoic basalts in eastern China is 78525 ± 3141 km^2 (*51*). The carbon stored at the bottom of the BMW, $C_{storage}$, can be calculated according to

$$C_{storage} = S_{total} \times h \times \rho \times C^{4+}$$

where h is thickness of EC basalt, ρ is the density of basalt, and C^{4+} is the amount of carbon required to elevate the average $Fe^{3+}/\sum Fe$ value of MORBs to what is observed in EC basalts via reaction of $4Fe^{2+} + C^{4+} \rightarrow 4Fe^{3+} + C^0$. We assume that the FeO_{total} content of EC basalt is 12 wt%, the density of basalt is 2.9 g/cm^3, and the thickness of EC basalt is ~10 km. To elevate the melt's $Fe^{3+}/\sum Fe$ from a MORB-like value 0.14 (*18*) to 0.35, the average of studied EC basalts (< 50 Ma), the $C_{storage}$ is roughly estimated to be 2400 Gt, which is four times of pre-industrial atmospheric carbon budget (Fig. S11). Note that the measured $Fe^{3+}/\sum Fe$ of EC basalts may represent a minimum value, because $Fe^{3+}/\sum Fe$ of EC basalts may be lowered as they ascended and percolated across the redox melting frontline (~250 km) through the redox melting reaction ($4Fe^{3+} + C^0 \rightarrow 4Fe^{2+} + C^{4+}$).

Supplementary Section 6

The data sources of HIMU lavas (St. Helena and Cook-Austral) used in Fig. 1 in the main text are listed in Supplementary Appendix 1.

The arc basalt data used in Fig. 3 in the main text are taken from GEOROC (http://georoc.mpch-mainz.gwdg.de/georoc/Entry.html), with data sources listed in Supplementary Appendix 2.

The best estimated 'most parental' $Fe^{3+}/\sum Fe$ values for OIB from each hotspot location used in Figs. 3 and 4 are from Brounce et al. (*19*), with original data from Hartley et al. (*104*), Shorttle et al. (*24*) (Iceland), Helz et al. (*105*), Brounce et al. (*106*), Moussallam et al. (*107*) (Hawaii), Moussallam et al. (*20*) (Erebus), Moussallam et al. (*2*) (Canaries and Cape Verde), Brounce et al. (*19*) and Gaborieau et al. (*108*) (Reunion). Elemental data source of OIB are provided in Supplementary Appendix 3. In order to minimize crystal fractionation/accumulation effects, OIB data are filtered by using lavas with MgO between 8% and 16%.

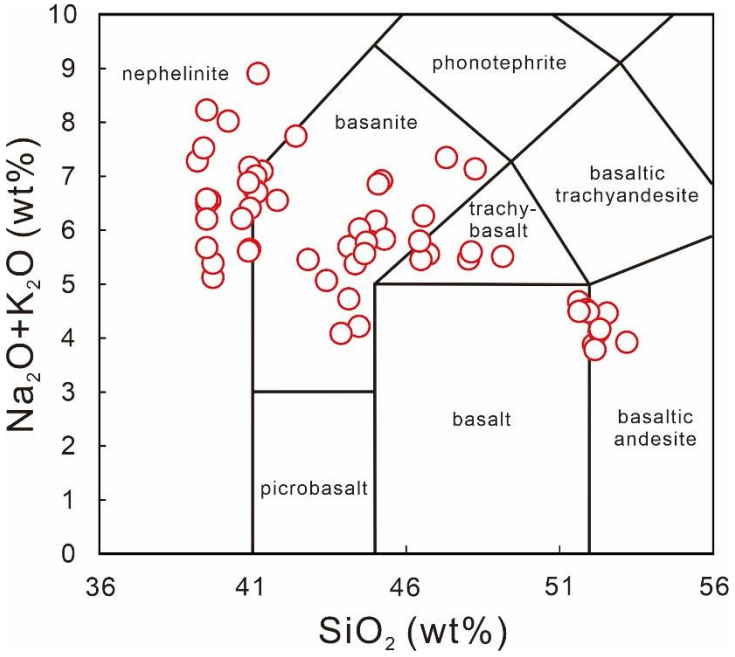

Fig. S1.
Total alkali ($Na_2O + K_2O$) vs SiO_2 diagram for EC Cenozoic intraplate basalts.

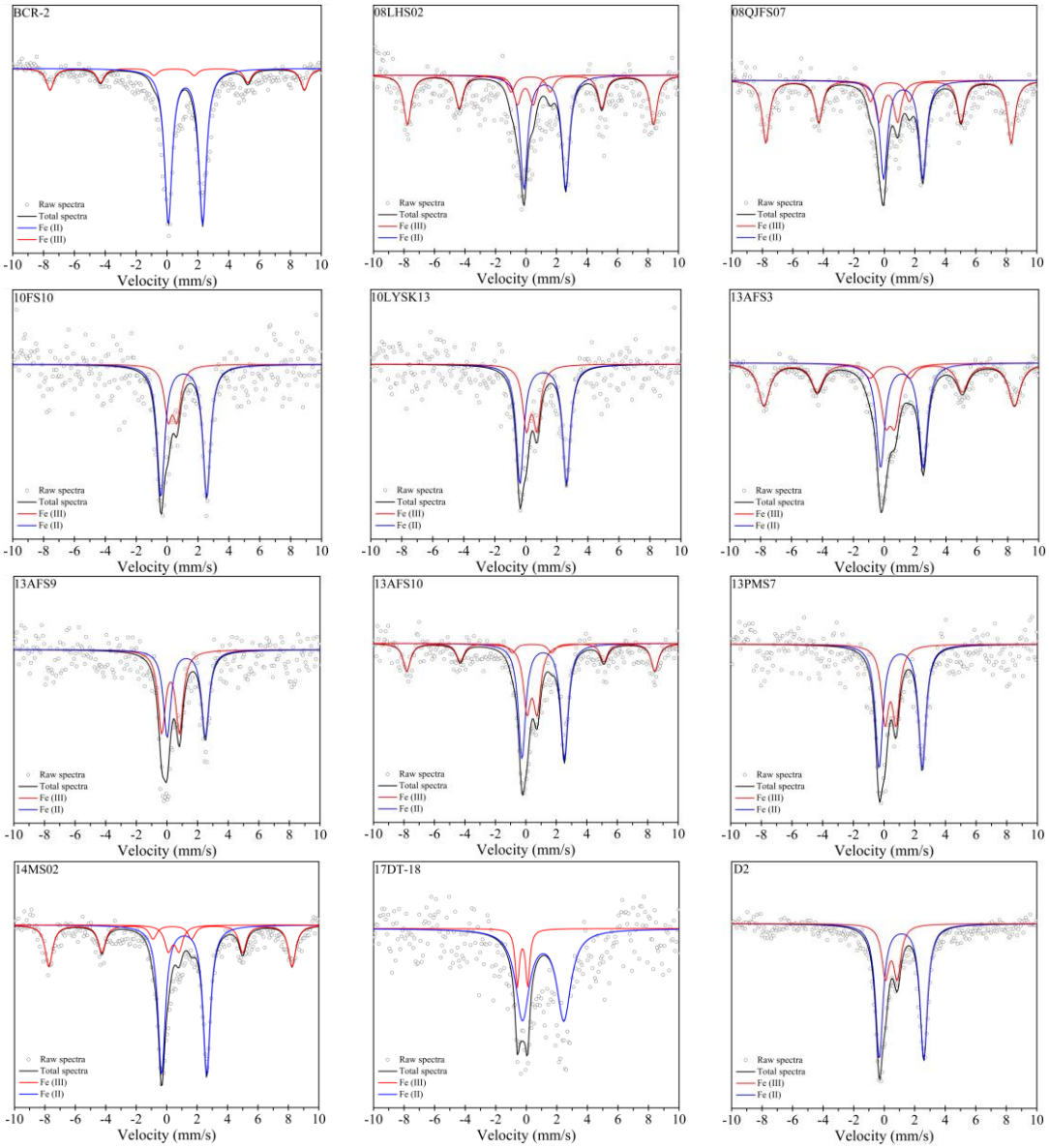

Fig. S2.

Mössbauer spectra measured at 12 K on all analyzed samples.

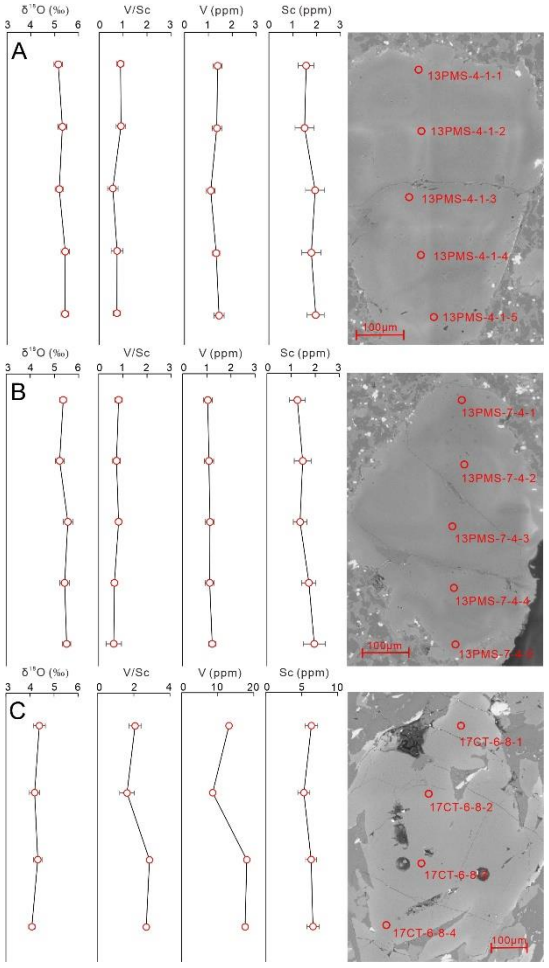

Fig. S3.

$\delta^{18}O$ values, V/Sc ratios, V and Sc content of different positions in olivine phenocrysts from the EC intraplate basalts. Data are reported in Table S4.

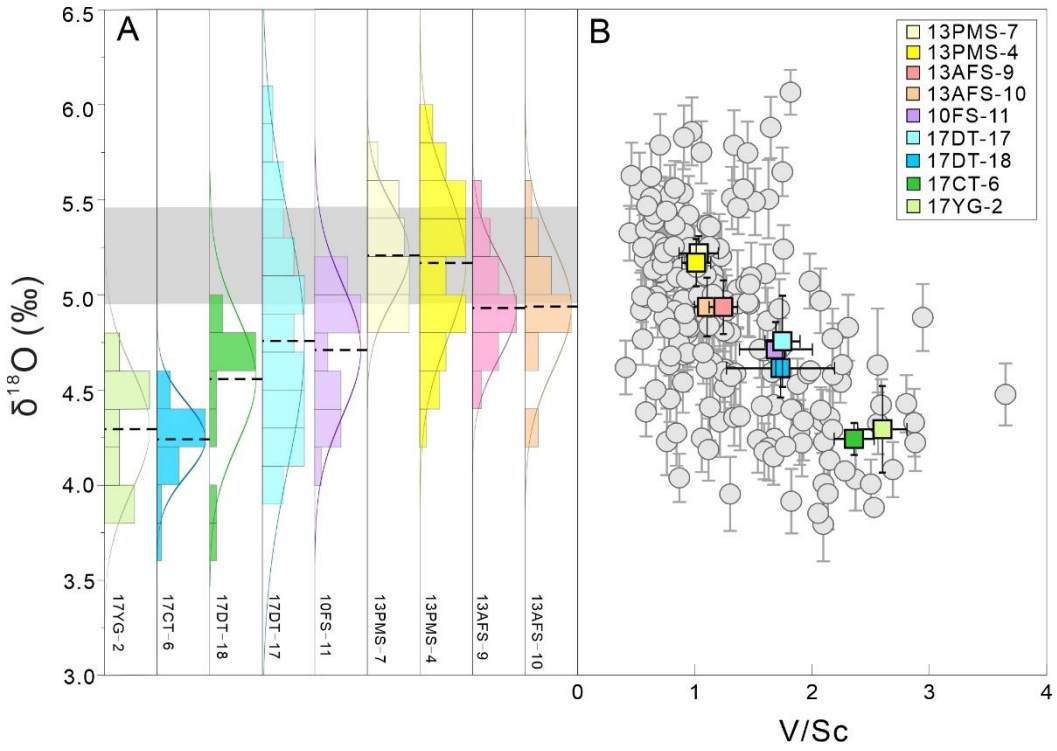

Fig. S4.

All analyzed olivine $\delta^{18}O$ and V/Sc in this study. (**A**) Probability distribution plots of oxygen isotope composition of olivine grains in each individual sample. The black dashed lines represent average $\delta^{18}O$ values for each probability distribution plot. Grey band represents the normal-mantle $\delta^{18}O$ value (5.18 ± 0.28 ‰) (*109*). (**B**) Covariation diagram of $\delta^{18}O$ versus V/Sc in olivine (n=198). Squares represent the average value of different samples. Error bars represent 2 s.e. Data are from Table S4.

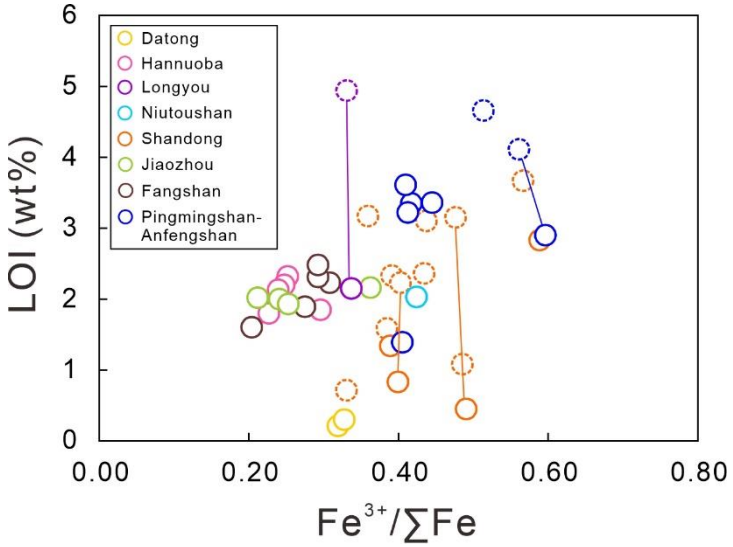

Fig. S5.

Measured $Fe^{3+}/\Sigma Fe$ versus Loss of Ignition (LOI) for EC Cenozoic intraplate basalts in different locations. The iddingsitized samples are shown in dashed outline. Fresh and iddingsitized samples from the same location are connected by lines. Note that the absence of correlation between $Fe^{3+}/\Sigma Fe$ and LOI, and no significant difference between fresh and iddingsitized samples, suggest that surface weathering (*e.g.,* iddingsitization) does not have a large impact on the bulk rock $Fe^{3+}/\Sigma Fe$ values.

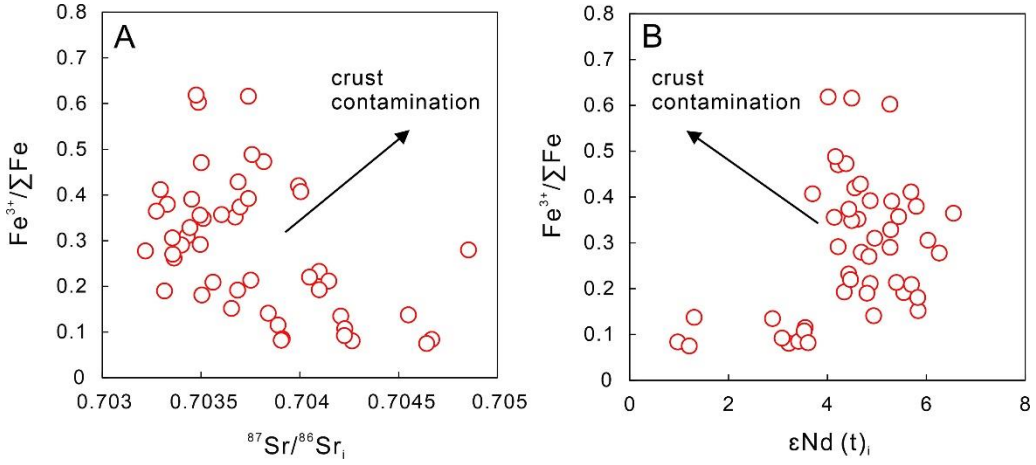

Fig. S6.

Corrected $Fe^{3+}/\Sigma Fe$ values versus $^{87}Sr/^{86}Sr_i$ (A) and $\varepsilon_{Nd}(t)_i$ (B) for EC Cenozoic intraplate basalts. Sr-Nd isotopic compositions were reported in Wang and Liu (*77*) and Li et al. (*16*) and references therein. The relationships preclude crustal contamination or AFC processes as the cause of elevated $Fe^{3+}/\Sigma Fe$ for the EC basalts.

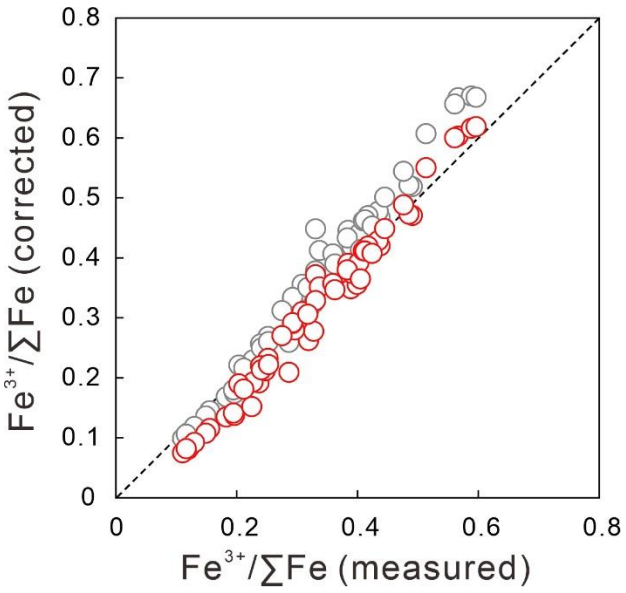

Fig. S7.

Olivine fractional crystallization or accumulation correction of $Fe^{3+}/\Sigma Fe$ for EC Cenozoic intraplate basalts compared with the measured $Fe^{3+}/\Sigma Fe$ value. Data are from Table S1. Samples equilibrium with mantle olivine at Fo_{90} are shown in red circles, and samples equilibrium with mantle olivine at Fo_{85} are shown in grey circles. Correction details are in the Supplementary Section 2.

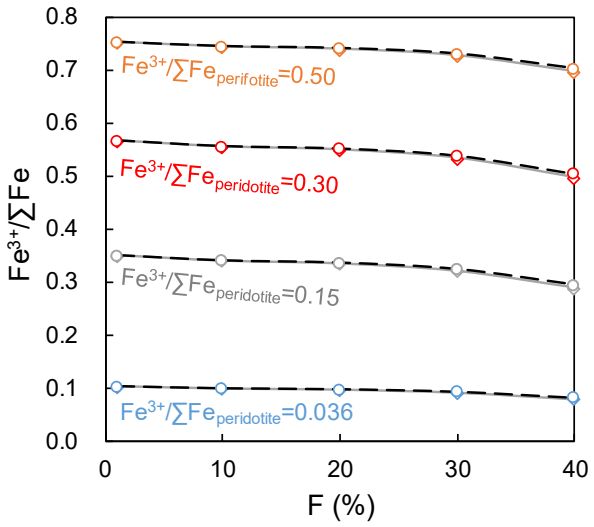

Fig. S8.

The $Fe^{3+}/\Sigma Fe$ of melts generated by batch (black dashed line) and fractional (grey solid line) partial melting of peridotites with different $Fe^{3+}/\Sigma Fe$. The peridotite sources are assumed to have initial $Fe^{3+}/\Sigma Fe$ of 0.036 (normal-mantle value) (*28*), 0.15, 0.30 and 0.50, respectively.

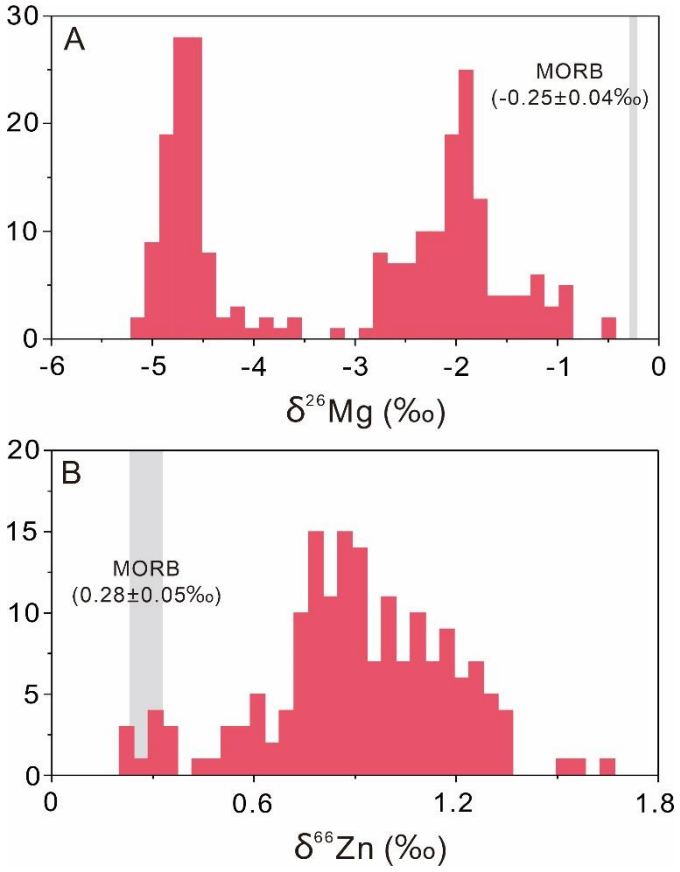

Fig. S9.

Magnesium (A) and Zinc (B) isotopic compositions of sedimentary carbonates compared to those of average MORB. δ^{26}Mg of sedimentary carbonates are compiled from Pokrovsky et al. (*110*), Geske et al. (*111*), Higgins and Schrag (*112-114*), Fantle and Higgins (*115*) and Blättler et al. (*116*). δ^{66}Zn of sedimentary carbonates are compiled from Pichat et al. (*117*), Liu et al. (*118*) and Sweere et al. (*119*). δ^{26}Mg and δ^{66}Zn of MORB shown in grey bar are from Teng et al. (*41*) and Chen et al. (*120*), respectively.

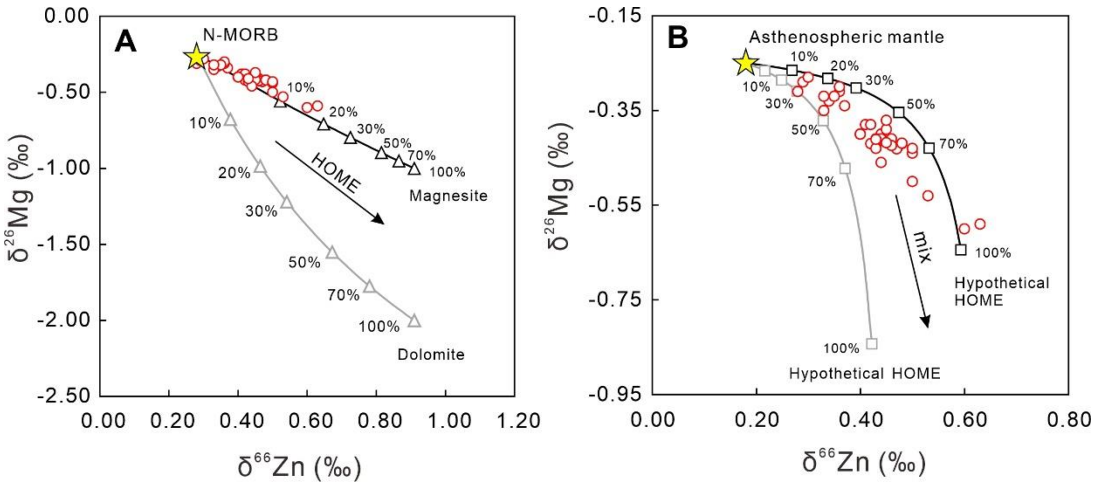

Fig. S10.

Plots of δ^{26}Mg against δ^{66}Zn for the EC intraplate basalts, together with MORB-carbonate mixing (A) and asthenospheric mantle-HOME mixing model (B). Two carbonate species including magnesite (black lines) and dolomite (grey lines) are considered. Hypothetical HOME in (B) is formed by hybridization of 15% carbonate and 85% N-MORB. Modelling parameters are provided in Supplementary Table 7.

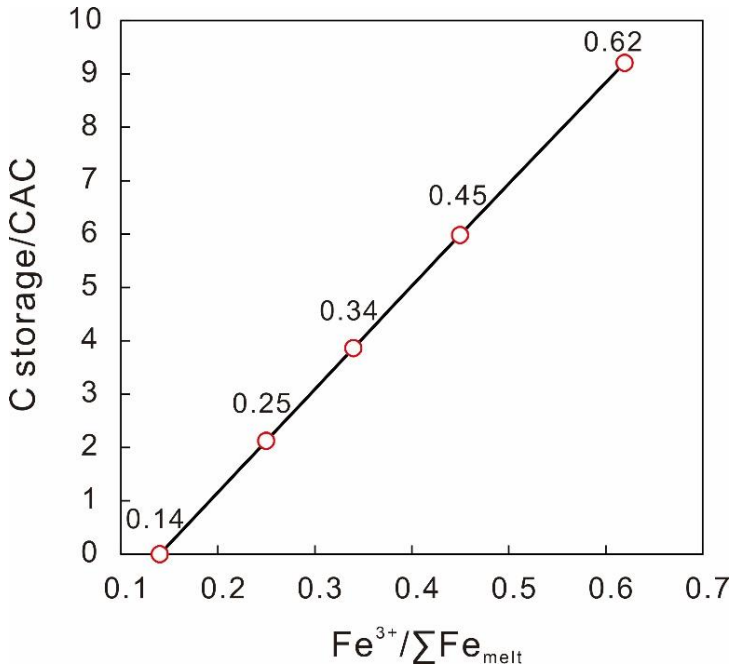

Fig. S11.

The total amount of carbon storage ($C_{storage}$) relative to the current atmospheric carbon (CAC) as a function of assumed average $Fe^{3+}/\Sigma Fe$ in EC Cenozoic intraplate basalts. Computation details are in the Supplementary Section 6.

Legends for Table S1 to S7

Table S1. Wet-chemical Fe^{3+}/Fe_{total} ratios for Cenozoic basalts from eastern China.

Table S2. Wet-chemical determination of FeO content in geological standards.

Table S3. Mössbauer spectroscopic measurements on samples at ~12 K and comparison with wet-chemical measurements.

Table S4. Oxygen isotope and V/Sc ratio of olivine in intraplate basalts from eastern China.

Table S5. The chemical compositions of modeled basaltic melts compared with those of molten basalt investigated by experiments and mid-ocean ridge basalt.

Table S6. The calculated density of three basaltic melts.

Table S7. Parameters used for mixing model.

Legends for Appendix 1 to 3

Appendix 1 Data sources of HIMU lavas.

Appendix 2 Data sources of arc basalts compiled from GEOROCK.

Appendix 3 Data sources of OIB lavas from each hotspot locations.

References

1. D. J. Frost, C. A. McCammon, The Redox State of Earth's Mantle. Annu. *Rev. Earth Planet. Sci.* **36**, 389-420 (2008).
2. Y. Moussallam, M.-A. Longpré, C. McCammon, A. Gomez-Ulla, E. F. Rose-Koga, B. Scaillet, N. Peters, E. Gennaro, R. Paris, C. Oppenheimer, Mantle plumes are oxidised. *Earth Planet. Sci. Lett*. **527**, 115798 (2019).
3. Y. S. He, X. Meng, S. Ke, H. Wu, C. Zhu, F.-Z. Teng, J. Hoefs, J. Huang, W. Yang, L. Xu, Z. Hou, Z.-Y. Ren, S. Li, A nephelinitic component with unusual δ^{56}Fe in Cenozoic basalts from eastern China and its implications for deep oxygen cycle. *Earth Planet. Sci. Lett*. **512**, 175-183 (2019).
4. R. W. Nicklas, R. K. M. Hahn, L. N. Willhite, M. G. Jackson, V. Zanon, R. Arevalo, J. M. D. Day, Oxidized mantle sources of HIMU- and EM-type Ocean Island Basalts. *Chem. Geol*. **602**, 120901 (2022).
5. S. C. Huang, O. Tschauner, S. Y. Yang, M. Humayun, W. J. Liu, S. N. G. Corder, H. A. Bechtel, J. Tischler, HIMU geochemical signature originating from the transition zone. *Earth Planet. Sci. Lett*. **542**, 116323 (2020).
6. E. S. Kiseeva, D. M. Vasiukov, B. J. Wood, C. McCammon, T. Stachel, M. Bykov, E. Bykova, A. Chumakov, V. Cerantola, J. W. Harris, L. Dubrovinsky, Oxidized iron in garnets from the mantle transition zone. *Nat. Geosci*. **11**, 144-147 (2018).
7. A. Rohrbach, M. W. Schmidt, Redox freezing and melting in the Earth's deep mantle resulting from carbon-iron redox coupling. *Nature* **472**, 209-212 (2011).
8. R. B. Tao, Y. W. Fei, Recycled calcium carbonate is an efficient oxidation agent under deep upper mantle conditions. *Commun. Earth Environ*. **2**, 1-8 (2021).
9. J. L. Huang, D. P. Zhao, High-resolution mantle tomography of China and surrounding regions. *J. Geophys. Res.* **111**, B09305 (2006).
10. E. Ohtani, D. Zhao, The role of water in the deep upper mantle and transition zone: dehydration of stagnant slabs and its effects on the big mantle wedge. *Russ. Geol. Geophys.* **50**, 1073-1078 (2009).
11. S. G. Li, Y. Wang, Formation time of the big mantle wedge beneath eastern China and a new lithospheric thinning mechanism of the North China craton-Geodynamic effects of deep recycled carbon. *Sci. China Earth Sci.* **61**, 853-868 (2018).
12. Q. Ma, Y.-G. Xu, Magmatic perspective on subduction of Paleo-Pacific plate and initiation of big mantle wedge in East Asia. *Earth Sci. Rev.* **213**, 103473 (2021).
13. Y. Xu, H. Li, L. Hong, L. Ma, Q. Ma, M. Sun, Generation of Cenozoic intraplate basalts in the big mantle wedge under eastern Asia. *Sci. China Earth Sci.* **61**, 869-886 (2018).
14. R. Xu, Y. Liu, X.-C. Wang, S. F. Foley, Y. Zhang, H. Yuan, Generation of continental intraplate alkali basalts and implications for deep carbon cycle. *Earth Sci. Rev.* **201**, 103073 (2020).
15. G. Zeng, L. H. Chen, X. S. Xu, S. Y. Jiang, A. W. Hofmann, Carbonated mantle sources for Cenozoic intra-plate alkaline basalts in Shandong, North China. *Chem. Geol.* **273**, 35-45 (2010).
16. S. G. Li, W. Yang, S. Ke, X. Meng, H. Tian, L. J. Xu, Y. S. He, J. Huang, X. C. Wang, Q. Xia, W. D. Sun, X. Y. Yang, Z. Y. Ren, H. Q. Wei, Y. S. Liu, F. C. Meng, J. Yan, Deep carbon cycles constrained by a large-scale mantle Mg isotope

anomaly in eastern China. *Nat. Sci. Rev.* **4**, 111-120 (2017).
17. Y. Liu, S. Gao, P. B. Kelemen, W. Xu, Recycled crust controls contrasting source compositions of Mesozoic and Cenozoic basalts in the North China Craton. *Geochim Cosmochim Ac* **72**, 2349-2376 (2008).
18. H. L. Zhang, E. Cottrell, P. A. Solheid, K. A. Kelley, M. M. Hirschmann, Determination of $Fe^{3+}/\sum Fe$ of XANES basaltic glass standards by Mössbauer spectroscopy and its application to the oxidation state of iron in MORB. *Chem. Geol.* **479**, 166-175 (2018).
19. M. Brounce, E. Stolper, J. Eiler, The mantle source of basalts from Reunion Island is not more oxidized than the MORB source mantle. *Contrib. to Mineral. Petrol.* **177**, 7 (2021).
20. Y. Moussallam, C. Oppenheimer, B. Scaillet, F. Gaillard, P. Kyle, N. Peters, M. Hartley, K. Berlo, A. Donovan, Tracking the changing oxidation state of Erebus magmas, from mantle to surface, driven by magma ascent and degassing. *Earth Planet. Sci. Lett.* **393**, 200-209 (2014).
21. D. Mattey, D. Lowry, C. Macpherson, Oxygen isotope composition of mantle peridotite. *Earth Planet. Sci. Lett.* **128**, 231-241 (1994).
22. C. T. A. Lee, W. P. Leeman, D. Canil, Z. X. A. Li, Similar V/Sc systematics in MORB and arc basalts: Implications for the oxygen fugacities of their mantle source regions. *J. Petrol.* **46**, 2313-2336 (2005).
23. K. A. Kelley, E. Cottrell, The influence of magmatic differentiation on the oxidation state of Fe in a basaltic arc magma. *Earth Planet. Sci. Lett.* **329**, 109-121 (2012).
24. O. Shorttle, Y. Moussallam, M. E. Hartley, J. Maclennan, M. Edmonds, B. J. Murton, Fe-XANES analyses of Reykjanes Ridge basalts: Implications for oceanic crust's role in the solid Earth oxygen cycle. *Earth Planet. Sci. Lett.* **427**, 272-285 (2015).
25. Y. Moussallam, G. Georgeais, E. F. Rose-Koga, K. T. Koga, M. E. Hartley, B. Scaillet, C. Oppenheimer, N. Peters, CO_2-Undersaturated Melt Inclusions From the South West Indian Ridge Record Surprisingly Uniform Redox Conditions. *Geochem. Geophys. Geosyst.* **24**, e2023GC011235 (2023).
26. G. A. Gaetani, The behavior of $Fe^{3+}/\sum Fe$ during partial melting of spinel lherzolite. *Geochim Cosmochim Ac* **185**, 64-77 (2016).
27. E. Cottrell, S. K. Birner, M. Brounce, F. A. Davis, L. E. Waters, K. A. Kelley, "*Oxygen Fugacity Across Tectonic Settings*" in *Magma Redox Geochemistry*, R. Moretti, D. R. Neuville, Eds (Wiley, 2021), pp. 33-61.
28. D. Canil, H. S. Oneill, D. G. Pearson, R. L. Rudnick, W. F. Mcdonough, D. A. Carswell, Ferric Iron in Peridotites and Mantle Oxidation-States. *Earth Planet. Sci. Lett.* **123**, 205-220 (1994).
29. Y. Moussallam, C. Oppenheimer, A. Aiuppa, G. Giudice, M. Moussallam, P. Kyle, Hydrogen emissions from Erebus volcano, Antarctica. *Bull. Volcanol.* **74**, 2109-2120 (2012).
30. F. Gaillard, B. Scaillet, M. Pichavant, G. Iacono-Marziano, The redox geodynamics linking basalts and their mantle sources through space and time. *Chem. Geol.* **418**, 217-233 (2015).
31. R. Moretti, D. R. Neuville, Eds. *Magma Redox Geochemistry* (American

Geophysical Union, Wiley 2022).
32. Y. Moussallam, M. Edmonds, B. Scaillet, N. Peters, E. Gennaro, I. Sides, C. Oppenheimer, The impact of degassing on the oxidation state of basaltic magmas: A case study of Kīlauea volcano. *Earth Planet. Sci. Lett.* **450**, 317-325 (2016).
33. S. Ding, T. Plank, P. J. Wallace, D. J. Rasmussen, Sulfur_X: A Model of Sulfur Degassing During Magma Ascent. *Geochem. Geophys. Geosyst.* **24**, e2022GC010552 (2023).
34. D. Canil, Vanadium partitioning and the oxidation state of Archaean komatiite magmas. *Nature* **389**, 842-845 (1997).
35. S. F. Foley, D. Prelevic, T. Rehfeldt, D. E. Jacob, Minor and trace elements in olivines as probes into early igneous and mantle melting processes. *Earth Planet. Sci. Lett.* **363**, 181-191 (2013).
36. K. A. Kelley, E. Cottrell, Water and the oxidation state of subduction zone magmas. *Science* **325**, 605-607 (2009).
37. T. Kogiso, Y. Tatsumi, S. Nakano, Trace element transport during dehydration processes in the subducted oceanic crust: 1. Experiments and implications for the origin of ocean island basalts. *Earth Planet. Sci. Lett.* **148**, 193-205 (1997).
38. M. J. Walter, G. P. Bulanova, L. S. Armstrong, S. Keshav, J. D. Blundy, G. Gudfinnsson, O. T. Lord, A. R. Lennie, S. M. Clark, C. B. Smith, L. Gobbo, Primary carbonatite melt from deeply subducted oceanic crust. *Nature* **454**, 622-625 (2008).
39. S. A. Liu, Z. Z. Wang, S. G. Li, J. Huang, W. Yang, Zinc isotope evidence for a large-scale carbonated mantle beneath eastern China. *Earth Planet. Sci. Lett.* **444**, 169-178 (2016).
40. F. Moynier, D. Vance, T. Fujii, P. Savage, The Isotope Geochemistry of Zinc and Copper. *Rev. Miner. Geochem.* **82**, 543-600 (2017).
41. F. Teng, Z., Magnesium Isotope Geochemistry. *Rev. Mineral. Geochem.* **82**, 219-287 (2017).
42. A. R. Thomson, M. J. Walter, S. C. Kohn, R. A. Brooker, Slab melting as a barrier to deep carbon subduction. *Nature* **529**, 76-79 (2016).
43. M. A. Kendrick, J. X. Zhao, Y. X. Feng, Early accretion and prolonged carbonation of the Pacific Ocean's oldest crust. *Geology* **50**, 1270-1275 (2022).
44. J. C. Alt, D. A. H. Teagle, Hydrothermal alteration of upper oceanic crust formed at a fast-spreading ridge: mineral, chemical, and isotopic evidence from ODP Site 801. *Chem. Geol.* **201**, 191-211 (2003).
45. Y. Weiss, C. Class, S. L. Goldstein, T. Hanyu, Key new pieces of the HIMU puzzle from olivines and diamond inclusions. *Nature* **537**, 666-670 (2016).
46. J. Y. Xu, A. Giuliani, Q. L. Li, K. Lu, J. C. Melgarejo, W. L. Griffin, Light oxygen isotopes in mantle-derived magmas reflect assimilation of sub-continental lithospheric mantle material. *Nat. Commun.* **12**, 6295 (2021).
47. X. C. Wang, S. A. Wilde, Q. L. Li, Y. N. Yang, Continental flood basalts derived from the hydrous mantle transition zone. *Nat. Commun.* **6**, 7700 (2015).
48. A. Rohrbach, C. Ballhaus, U. Golla-Schindler, P. Ulmer, V. S. Kamenetsky, D. V. Kuzmin, Metal saturation in the upper mantle. *Nature* **449**, 456-458 (2007).
49. S. E. Mazza, E. Gazel, M. Bizimis, R. Moucha, P. Beguelin, E. A. Johnson, R. J. McAleer, A. V. Sobolev, Sampling the volatile-rich transition zone beneath

Bermuda. *Nature* **569**, 398-403 (2019).
50. P. R. Castillo, The recycling ofmarine carbonates and sources of HIMU and FOZO ocean island basalts. *Lithos* **216**, 254-263 (2015).
51. X. Y. Chen, L. H. Chen, Y. Chen, G. Zeng, J. Q. Liu, Distribution Summary of Cenozoic Basalts in Central and Eastern China. *Geological Journal of China Universities* **20**, 507-519 (2014).
52. V. Stagno, D. O. Ojwang, C. A. McCammon, D. J. Frost, The oxidation state of the mantle and the extraction of carbon from Earth's interior. *Nature* **493**, 84-88 (2013).
53. S. F. Foley, "*Redox Melting in the Mantle*" in *Magma Redox Geochemistry*, R. Moretti, D. R. Neuville, Eds (Wiley, 2021), pp. 93-113.
54. Y. Fukao, M. Obayashi, Subducted slabs stagnant above, penetrating through, and trapped below the 660 km discontinuity. *J Geophys Res-Sol Ea* **118**, 5920-5938 (2013).
55. M. Yin, J. X. Li, Eds. *Analysis of Rock and Minerals* (Geological Publishing House, Beijing 2011), vol. 2, pp. 1–862 (in Chinese).
56. P. A. Sossi, J. D. Foden, G. P. Halverson, Redox-controlled iron isotope fractionation during magmatic differentiation: an example from the Red Hill intrusion, S. Tasmania. *Contrib. to Mineral. Petrol.* **164**, 757-772 (2012).
57. A. Kumar, M. R. Singh, P. R. Sarma, K. C. Tripathi, Optimized Thickness of Diffusive Mossbauer Absorbers. *J. Phys. D. Appl. Phys.* **22**, 465-466 (1989).
58. A. Thompson, D. G. Rancourt, O. A. Chadwick, J. Chorover, Iron solid-phase differentiation along a redox gradient in basaltic soils. *Geochim Cosmochim Ac* **75**, 119-133 (2011).
59. T. Mansfeldt, S. Schuth, W. Hausler, F. E. Wagner, S. Kaufhold, M. Overesch, Iron oxide mineralogy and stable iron isotope composition in a Gleysol with petrogleyic properties. *J. Soil Sedim.* **12**, 97-114 (2012).
60. J. M. Eiler, C. Graham, J. W. Valley, SIMS analysis of oxygen isotopes: matrix effects in complex minerals and glasses. *Chem. Geol.* **138**, 221-244 (1997).
61. F. Guo, J. T. Guo, C. Y. Wang, W. M. Fan, C. W. Li, L. Zhao, H. X. Li, J. Y. Li, Formation of mafic magmas through lower crustal AFC processes - An example from the Jinan gabbroic intrusion in the North China Block. *Lithos* **179**, 157-174 (2013).
62. J. Eiler, E. M. Stolper, M. C. McCanta, Intra- and Intercrystalline Oxygen Isotope Variations in Minerals from Basalts and Peridotites. *J. Petrol.* **52**, 1393-1413 (2011).
63. N. T. Kita, T. Ushikubo, B. Fu, M. J. Spicuzza, J. W. Valley, Analytical developments on oxygen three isotope analyses using a new generation ion microprobe IMS-1280. *Lunar and Planetary Science XXXVIII* (1981), (2007).
64. I. Bindeman, A. Gurenko, O. Sigmarsson, M. Chaussidon, Oxygen isotope heterogeneity and disequilibria of olivine crystals in large volume Holocene basalts from Iceland: Evidence for magmatic digestion and erosion of Pleistocene hyaloclastites. *Geochim Cosmochim Ac* **72**, 4397-4420 (2008).
65. A. A. Gurenko, I. N. Bindeman, M. Chaussidon, Oxygen isotope heterogeneity of the mantle beneath the Canary Islands: insights from olivine phenocrysts. *Contrib. to Mineral. Petrol.* **162**, 349-363 (2011).

66. S. T. Wu, G. Worner, K. P. Jochum, B. Stoll, K. Simon, A. Kronz, The Preparation and Preliminary Characterisation of Three Synthetic Andesite Reference Glass Materials (ARM-1, ARM-2, ARM-3) for In Situ Microanalysis. *Geostand. Geoanal. Res.* **43**, 567-584 (2019).
67. V. G. Batanova, J. M. Thompson, L. V. Danyushevsky, M. V. Portnyagin, D. Garbe-Schonberg, E. Hauri, J. I. Kimura, Q. Chang, R. Senda, K. Goemann, C. Chauvel, S. Campillo, D. A. Ionov, A. V. Sobolev, New Olivine Reference Material for In Situ Microanalysis. *Geostand. Geoanal. Res.* **43**, 453-473 (2019).
68. S. T. Wu, Y. D. Wu, Y. H. Yang, H. Wang, C. Huang, L. W. Xie, J. H. Yang, Simultaneous Quantification of Forsterite Content and Minor-Trace Elements in Olivine by LA-ICP-MS and Geological Applications in Emeishan Large Igneous Province. *Minerals-Basel* **10**, 634 (2020).
69. W. F. McDonough, S. s. Sun, The composition of the Earth. *Chem. Geol.* **120**, 223-253 (1995).
70. R. L. Rudnick, S. Gao, "*Composition of the Continental Crust*" in *Treatise on Geochemistry*, H. D. Holland, K. K. Turekian, Eds (Pergamon, 2003), vol. 3, pp. 1–64.
71. Y. Weiss, W. L. Griffin, D. R. Bell, O. Navon, High-Mg carbonatitic melts in diamonds, kimberlites and the sub-continental lithosphere. *Earth Planet. Sci. Lett.* **309**, 337-347 (2011).
72. K. Hoernle, G. Tilton, M. J. Le Bas, S. Duggen, D. Garbe-Schönberg, Geochemistry of oceanic carbonatites compared with continental carbonatites: mantle recycling of oceanic crustal carbonate. *Contrib. Mineral. Petrol.* **142**, 520-542 (2002).
73. J. W. Valley, M. J. Spicuzza, T. Ushikubo, Correlated $\delta^{18}O$ and [Ti] in lunar zircons: a terrestrial perspective for magma temperatures and water content on the Moon. *Contrib. Miner. Petrol.* **167**, 956 (2014).
74. A. Fitzpayne, A. Giuliani, J. Hergt, D. Phillips, P. Janney, New geochemical constraints on the origins of MARID and PIC rocks: Implications for mantle metasomatism and mantle-derived potassic magmatism. *Lithos* **318**, 478-493 (2018).
75. M. Massuyeau, X. Ritter, C. Sanchez-Valle, A density model for high-pressure carbonate-rich melts applied to carbonatitic magmatism in the upper mantle. *Chem. Geol.* **622**, 121275 (2022).
76. R. Dasgupta, Ingassing, Storage, and Outgassing of Terrestrial Carbon through Geologic Time. *Rev. Miner. Geochem.* **75**, 183-229 (2013).
77. Z. Z. Wang, S. A. Liu, Evolution of Intraplate Alkaline to Tholeiitic Basalts via Interaction Between Carbonated Melt and Lithospheric Mantle. *J. Petrol.* **62**, 1-25 (2021).
78. S. P. Qian, Z. Y. Ren, L. Zhang, L. B. Hong, J. Q. Liu, Chemical and Pb isotope composition of olivine-hosted melt inclusions from the Hannuoba basalts, North China Craton: Implications for petrogenesis and mantle source. *Chem. Geol.* **401**, 111-125 (2015).
79. G. Zeng, L. H. Chen, A. W. Hofmann, X. J. Wang, J. Q. Liu, X. Yu, L. W. Xie, Nephelinites in eastern China originating from the mantle transition zone. *Chem. Geol.* **576**, 120276 (2021).

80. J. Huang, S.-G. Li, Y. Xiao, S. Ke, W.-Y. Li, Y. Tian, Origin of low $\delta^{26}Mg$ Cenozoic basalts from South China Block and their geodynamic implications. *Geochim Cosmochim Ac* **164**, 298-317 (2015).
81. F. C. Meng, T. F. Li, H. M. Xue, F. L. Liu, Z. Q. Xu, Two serials of basic magmas from different mantle sources of Late Cretaceous in east Shandong province, China: a comparative study on basalts from Zhucheng and Jiaozhou. *Acta Petrologica Sinica* **22**, 1644-1656 (in Chinese with English abstract) (2006).
82. J. Yang, Petrological and Geochemical studies of the Cenozoic Basalts and Hosted Peridotite Xenoliths in Zhejiang and Fujian Provinces Ph.D. *China University of Geosciences (Beijing)*, (2015).
83. C. Q. Sun, J. Q. Liu, B. Xu, H. T. You, First radiocarbon dating of a Holocene eruption of the Datong volcanic field, eastern China. *J. Volcanol. Geotherm. Res.* **384**, 275-279 (2019).
84. H. Zhao, Z. Liu, C. M. Wang, S. H. Li, Luminescence dating of volcanic eruptions in Datong, northern China. *Quat Geochronol* **30**, 357-362 (2015).
85. D. Luo, L. H. Chen, G. Zeng, Genesis of intra-continental strongly alkaline volcanic rocks: A case study of Dashan neohelinites in Wudi, Shandong Province, North China. *Acta Petrologica Sinica* **25**, 311-319 (in Chinese with English abstract) (2009).
86. S. Z. Sheng, S. J. Wang, X. M. Yang, L. H. Chen, G. Zeng, Y. Xiao, J. Shen, X. H. Dong, Y. W. Lv, Sulfide Dissolution on the Nickel Isotopic Composition of Basaltic Rocks. *J. Geophys. Res. Solid Earth* **127**, e2022JB024555 (2022).
87. Z. Z. Wang, S. A. Liu, L. H. Chen, S. G. Li, G. Zeng, Compositional transition in natural alkaline lavas through silica-undersaturated melt–lithosphere interaction. *Geology* **46**, 771-774 (2018).
88. E. Cottrell, K. A. Kelley, The oxidation state of Fe in MORB glasses and the oxygen fugacity of the upper mantle. *Earth Planet. Sci. Lett.* **305**, 270-282 (2011).
89. P. A. Sossi, O. Nebel, J. Foden, Iron isotope systematics in planetary reservoirs. *Earth Planet. Sci. Lett.* **452**, 295-308 (2016).
90. P. L. Roeder, R. F. Emslie, Olivine-Liquid Equilibrium. *Contrib. to Mineral. Petrol.* **29**, 275–289 (1970).
91. A. D. T. Goode, Oxidation of natural olivines. *Nature* **248**, 500-501 (1974).
92. H. M. Williams, M. Bizimis, Iron isotope tracing of mantle heterogeneity within the source regions of oceanic basalts. *Earth Planet. Sci. Lett.* **404**, 396-407 (2014).
93. M. J. Walter, Melting of garnet peridotite and the origin of komatiite and depleted lithosphere. *J. Petrol.* **39**, 29-60 (1998).
94. J. Wang, F. Huang, X. Xiong, E. Takahashi, "*Partition Coefficients of Fe^{3+} and Fe^{2+} between Mantle Minerals and Melts: Implications for Redox Variations during Mantle Melting"* (AGU Fall Meeting 2021, New Orleans, LA, 2021).
95. R. Dasgupta, M. M. Hirschmann, The deep carbon cycle and melting in Earth's interior. *Earth Planet. Sci. Lett.* **298**, 1-13 (2010).
96. B. B. Karki, First-principles computation of mantle materials in crystalline and amorphous phases. *Phys. Earth Planet.* **240**, 43-69 (2015).
97. R. Wentzcovitch, L. Stixrude, J. J. Rosso, "*Thermodynamic properties and phase relations in mantle minerals investigated by first principles Quasiharmonic*

theory. " in *Theoretical and computational methods in mineral physics: Geophysical applications,* R. Wentzcovitch, L. Stixrude, Eds (Berlin, Boston, 2010).
98. W. Wang, Y. Xu, D. Sun, S. Ni, R. Wentzcovitch, Z. Wu, Velocity and density characteristics of subducted oceanic crust and the origin of lower-mantle heterogeneities. *Nat. Commun.* **11**, 64 (2020).
99. R. Caracas, K. Hirose, R. Nomura, M. D. Ballmer, Melt–crystal density crossover in a deep magma ocean. *Earth Planet. Sci. Lett.* **516**, 202-211 (2019).
100. C. B. Agee, Crystal-liquid density inversions in terrestrial and lunar magmas. *Phys. Earth Planet. In.* **107**, 63-74 (1998).
101. J. W. E. Drewitt, M. J. Walter, J. P. Brodholt, J. M. R. Muir, O. T. Lord, Hydrous silicate melts and the deep mantle H_2O cycle. *Earth Planet. Sci. Lett.* **581**, 117408 (2022).
102. N. V. Solomatova, R. Caracas, Buoyancy and Structure of Volatile-Rich Silicate Melts. *J. Geophys. Res. Solid Earth* **126**, e2020JB021045 (2021).
103. N. V. Solomatova, R. Caracas, C. E. Manning, Carbon sequestration during core formation implied by complex carbon polymerization. *Nat. Commun.* **10**, 789 (2019).
104. M. E. Hartley, O. Shorttle, J. Maclennan, Y. Moussallam, M. Edmonds, Olivine-hosted melt inclusions as an archive of redox heterogeneity in magmatic systems. *Earth Planet. Sci. Lett.* **479**, 192-205 (2017).
105. R. L. Helz, E. Cottrell, M. Brounce, K. A. Kelley, Olivine-melt relationships and syneruptive redox variations in the 1959 eruption of Kīlauea Volcano as revealed by XANES. *J. Volcanol. Geotherm. Res.* **333**, 1-14 (2017).
106. M. Brounce, E. Stolper, J. Eiler, Redox variations in Mauna Kea lavas, the oxygen fugacity of the Hawaiian plume, and the role of volcanic gases in Earth's oxygenation. *Proc. Natl. Acad. Sci. U. S. A.* **114**, 8997-9002 (2017).
107. Y. Moussallam, M. Edmonds, B. Scaillet, N. Peters, E. Gennaro, I. Sides, C. Oppenheimer, The impact of degassing on the oxidation state of basaltic magmas: A case study of Kīlauea volcano. *Earth Planet. Sci. Lett.* **450**, 317-325 (2016).
108. M. Gaborieau, M. Laubier, N. Bolfan-Casanova, C. A. McCammon, D. Vantelon, A. I. Chumakov, F. Schiavi, D. R. Neuville, S. Venugopal, Determination of $Fe^{3+}/\Sigma Fe$ of olivine-hosted melt inclusions using Mössbauer and XANES spectroscopy. *Chem. Geol.* **547**, 119646 (2020).
109. D. Mattey, D. Lowry, C. Macpherson, Oxygen isotope composition of mantle peridotite. *Earth Planet. Sci. Lett.* **128**, 231-241 (1994).
110. B. G. Pokrovsky, V. Mavromatis, O. S. Pokrovsky, Co-variation of Mg and C isotopes in late Precambrian carbonates of the Siberian Platform: A new tool for tracing the change in weathering regime? *Chem. Geol.* **290**, 67-74 (2011).
111. A. Geske, J. Zorlu, D. K. Richter, D. Buhl, A. Niedermayr, A. Immenhauser, Impact of diagenesis and low grade metamorphosis on isotope ($\delta^{26}Mg$, $\delta^{13}C$, $\delta^{18}O$ and $^{87}Sr/^{86}Sr$) and elemental (Ca, Mg, Mn, Fe and Sr) signatures of Triassic sabkha dolomites. *Chem. Geol.* **332-333**, 45-64 (2012).
112. J. A. Higgins, D. P. Schrag, Constraining magnesium cycling in marine sediments using magnesium isotopes. *Geochim Cosmochim Ac* **74**, 5039-5053 (2010).
113. J. A. Higgins, D. P. Schrag, The Mg isotopic composition of Cenozoic seawater-

evidence for a link between Mg-clays, seawater Mg/Ca, and climate. *Earth Planet. Sci. Lett.* **416**, 73-81 (2015).
114. J. A. Higgins, D. P. Schrag, Records of Neogene seawater chemistry and diagenesis in deep-sea carbonate sediments and pore fluids. *Earth Planet. Sci. Lett.* **357**, 386-396 (2012).
115. M. S. Fantle, J. Higgins, The effects of diagenesis and dolomitization on Ca and Mg isotopes in marine platform carbonates: Implications for the geochemical cycles of Ca and Mg. *Geochim Cosmochim Ac* **142**, 458-481 (2014).
116. C. L. Blattler, N. R. Miller, J. A. Higgins, Mg and Ca isotope signatures of authigenic dolomite in siliceous deep-sea sediments. *Earth Planet. Sci. Lett.* **419**, 32-42 (2015).
117. S. Pichat, C. Douchet, F. Albarède, Zinc isotope variations in deep-sea carbonates from the eastern equatorial Pacific over the last 175 ka. *Earth Planet. Sci. Lett.* **210**, 167-178 (2003).
118. S. A. Liu, H. C. Wu, S. Z. Shen, G. Q. Jiang, S. H. Zhang, Y. W. Lv, H. Zhang, S. G. Li, Zinc isotope evidence for intensive magmatism immediately before the end-Permian mass extinction. *Geology* **45**, 343-346 (2017).
119. T. C. Sweere, A. J. Dickson, H. C. Jenkyns, D. Porcelli, M. Elrick, S. H. J. M. van den Boorn, G. M. Henderson, Isotopic evidence for changes in the zinc cycle during Oceanic Anoxic Event 2 (Late Cretaceous). *Geology* **46**, 463-466 (2018).
120. H. Chen, P. S. Savage, F.-Z. Teng, R. T. Helz, F. Moynier, Zinc isotope fractionation during magmatic differentiation and the isotopic composition of the bulk Earth. *Earth Planet. Sci. Lett.* **369-370**, 34-42 (2013).